Supplementary Information

Copper nanoparticle ensembles for selective electroreduction of CO_2 to C_2-C_3 products

Dohyung Kim[a,c,d], Christopher S. Kley[b], Yifan Li[b,c,d], Peidong Yang[a,b,c,d,1]

[a]Department of Materials Science and Engineering, University of California, Berkeley, California 94720, United States.

[b]Department of Chemistry, University of California, Berkeley, California 94720, United States.

[c]Chemical Sciences Division, Lawrence Berkeley National Laboratory, Berkeley, California 94720, United States.

[d]Kavli Energy NanoScience Institute, Berkeley, California 94720, United States.

[1]Correspondence to: p_yang@berkeley.edu

Contents

Methods

Materials. Trioctylamine (98%), oleylamine (70%), copper (I) acetate (97%), tetradecylphosphonic acid (97%), trioctylphosphine oxide (90%), copper (I) bromide (99.999%, trace metals basis) and cesium carbonate (99.995%, trace metals basis) were purchased from Sigma-Aldrich. Potassium carbonate (99.997%, trace metals basis) was purchased from Alfa Aesar. Highly polished graphite was purchased from Ted Pella and carbon paper (Sigracet, GDL35) was purchased from Ion Power. Ag/AgCl electrodes were purchased from CH Instruments and World Precision Instruments. Hg/HgO electrode was purchased from CH Instruments. Carbon dioxide (5.0 UHP) and Argon (5.0 UHP) gas were purchased from Praxair. Deionized water was from a Millipore system. All reagents were of analytical grade and used without further purification.

Copper nanoparticle synthesis and the formation of copper nanoparticle ensembles on carbon paper support. Cu nanoparticles were synthesized by the reduction of copper (I) acetate (CuAc) precursor at high temperatures. 0.1226g of CuAc and 0.1392g of tetradecylphosphonic acid (TDPA) were added to pre-heated (130°C for 30 minutes under nitrogen atmosphere) trioctylamine solvent (10ml) at room temperature. While stirring and keeping it under N_2, the solution was heated to 180°C and then to 270°C, with 30 minute periods at each temperature point. Subsequently, the heat source was disconnected and the solution was cooled to 100°C. Ethanol was added and the solution mixture was centrifuged at 6000 rpm for 15 minutes. Separated nanoparticles were washed more with chloroform and acetone mixtures and finally redispersed in hexane for further use and characterization.

Cu nanoparticle stock solution in hexane (0.53mg/ml) was used to form varied density of Cu nanoparticle ensembles on carbon paper support. Cu nanoparticles were directly deposited onto carbon paper (1 cm^2_{geo}), with the loadings multiply varied starting from 2.12 μg of copper mass (×1 loading). The volume of single deposition was carefully controlled not to exceed its area (1cm^2_{geo}) and the total volume was set according to the targeted loading amount.

For intentionally separating the high density Cu nanoparticle ensembles, Ketjen black was mixed with Cu nanoparticles in hexane (C/Cu mass ratio 8) before directly depositing onto carbon paper. When using highly polished graphite plate (roughness factor ~1) as a support material, Cu nanoparticles were deposited in the same manner, while keeping the loading density (NPs/cm^2_{real}) consistent.

Characterization. Cu nanoparticles were characterized by TEM (Hitachi H-7650) and XRD (Bruker D8). TEM grids were prepared by directly dropping a dilute solution of Cu NPs (in hexane) onto a carbon film grid. Cu NP ensembles on carbon paper were imaged by SEM (Ultra 55-FESEM). XPS (PHI 5400) measurements were carried out using a Mg Kα source, with the pressure inside the chamber maintained below ~ 4×10^{-9} Torr and spectra collected at pass energy of 17.9 eV. For quantification, collected spectra were corrected using a Shirley background.

Surface area measurements of carbon supports. Real surface areas of carbon supports

were estimated by probing the redox reaction of ferricyanide/ferrocyanide using cyclic voltammetry (CV). Various types of carbon supports were wetted before analysis. 0.1 M KCl solution containing 1 mM ferricyanide was initially degassed with Ar. Then, while keeping the solution still, potential of the working electrode was sweeped between 600 mV and -200 mV vs Ag/AgCl (1 M KCl) at various scan rates (mV/s). Between the scans at different rates, the solution was bubbled with Ar and agitated to quickly reach back to the initial condition.

Surface areas were estimated from Randles-Sevcik equation. Randles-Sevcik equation is as follows,

$$I_p = (2.69 \times 10^5)\, n^{3/2} A D^{1/2} v^{1/2} C$$

I_p : peak current
n : number of moles of electrons per mole of electroactive species
A : area of electrode (cm^2) D : diffusion coefficient (cm^2/s)
v : scan rate (V/s) C : concentration (mol/cm^3)

Diffusion coefficient of ferricyanide is 6.7×10^{-6} cm^2/s and the concentration used in this work is 10^{-6} mol/cm^3. By plotting I_p versus $v^{1/2}$ and measuring the slope, area (A) can be estimated. To experimentally confirm the validity of this approach, test measurements were performed on glassy carbon electrodes and highly polished graphite plates (with other unpolished sections sealed from the electrolyte) and the areas estimated were in close match to their expected areas. The same procedure was followed for carbon paper with geometric area $1cm^2$ to estimate its roughness factor and real surface area.

CO_2 reduction electrochemical measurements. All electrochemical measurements were

carried out in a customized setup, which has two compartments separated by an anion exchange membrane (Selemion, AMV). Each compartment contains 15 ml of electrolyte and the compartment that holds the working electrode is sealed to measure gaseous products. Platinum wire is used as a counter electrode and a Ag/AgCl (WPI, 3M KCl) is used as a reference. The potential of Ag/AgCl (WPI, 3M KCl) electrode was routinely checked against fresh Ag/AgCl (CHI, 1M KCl) and Hg/HgO (CHI, 1M NaOH), which yielded potential differences of -24 ± 4 mV and 75 ± 6 mV, respectively. All potentials measured are converted to RHE scale by V (vs. RHE) = V (vs. Ag/AgCl, 3M KCl) + 0.210 V + 0.0591 × pH. 0.1M bicarbonate electrolytes used were prepared by bubbling carbonate salt solutions overnight with CO_2.

Before electrolysis, electrolyte was saturated with CO_2 at a flow rate of 20 sccm for 15 ~ 20 minutes while stirring. Linear sweep voltammetry (at scan rate of 50 mV/s) was performed initially and then a set potential was applied for chronoamperometry. The solution resistance was compensated for 84% by the potentiostat (Biologic) and the rest 16% was post-corrected. During constant potential electrolysis (1hr), effluent gas from the working compartment went through the sampling loop of a gas chromatograph (SRI GC) for product analysis. Gas chromatograph is equipped with a molecular sieve 13X (1/8” × 6’) and hayesep D (1/8” × 6’) column with Ar flowing as a carrier gas. Sample for gas chromatography was collected at 20 minute intervals and the separated gas products were analyzed by a thermal conductivity detector (for H_2) and a flame ionization detector (for CO and hydrocarbons). Quantification of the products was performed with the conversion factor derived from the standard calibration gases and the concentration of gas measured was further converted to partial current density. Liquid products were analyzed afterwards by qNMR (Bruker AV-700) using

dimethyl sulfoxide as an internal standard. Solvent presaturation technique was implemented to suppress the water peak. Faradaic efficiencies (FE) were calculated from the amount of charge passed to produce each product divided by the total charge passed at a specific time (gas) or during the overall run (liquid).

For electrochemical measurements of trans-CuEn (×22.5 loaded carbon paper) in 0.1 M $KHCO_3$ saturated with 1 atm CO_2 at various potentials, -0.81 V vs. RHE is first applied for 7 min and then stepped to the relevant potential of interest. Potentials more negative then mentioned here were applied directly at the start of electrolysis. For trans-CuEn 2 (×32.5 loaded carbon paper in 0.1 M $CsHCO_3$) at various potentials, -0.75 V vs. RHE is first applied for 7 min and then stepped to the relevant potential of interest. Sum of all product FEs for each measurement was ~94 ± 3% and normalized afterwards. Error bars shown are one standard deviation from three independent sample measurements.

Double layer capacitance measurements. Double layer capacitance measurements were performed on the structurally transformed Cu nanoparticle ensembles after electrolysis. Using Ar saturated 0.1 M $KHCO_3$, CV were taken between -0.3 and -0.6 V vs. Ag/AgCl (3M KCl) at various scan rates (mV/s). Measurement performed on carbon paper support ($1cm^2_{geo}$) resulted in capacitance value of 254 μF. In addition, 36 μF was measured for electropolished copper foil ($1cm^2_{geo}$). Capacitance values measured for different loading conditions were subtracted with the capacitance of bare carbon paper support, assuming underlying carbon paper support would be electrochemically accessible, and divided by 36μF to estimate the real surface area of structurally transformed Cu nanoparticles. Identical procedures were

followed in Ar saturated 0.1 M $CsHCO_3$ as well. Measured values for carbon paper support ($1cm^2_{geo}$) and electropolished copper foil ($1cm^2_{geo}$) were 499 μF and 43 μF, respectively.

CO_2 reduction measurements with copper nanocubes. Cu nanocubes were synthesized following procedures from previous report (1). To obtain 40 nm cubes, 0.6 mmol of copper (I) bromide (CuBr) and 1.5 mmol of trioctylphosphine oxide (TOPO) were added to oleylamine (7 ml). Then the mixture was heated to 80 °C for 15 min under Ar atmosphere. After dissolution of both chemicals, the solution was ramped to 260 °C and refluxed for 1 hour. Then, the solution was cooled down to room temperature. For the Cu nanocubes of 25 nm size, 0.6 mmol of CuBr, 5 mmol of TOPO and 2 ml of oleylamine were used. In addition, 1 hr reflux was done at 210 °C before cooling down to room temperature. As-synthesized nanocubes were washed 3 times in a mixture of hexane and acetone (1:1) by centrifugation and resuspended in hexane for further use.

To check the catalytic activity of Cu nanocubes, 40 nm cubes were tested in an identical manner to the previous report (1) by depositing them on a glassy carbon plate. These measurements resulted in similar activities to the previous report. For the comparison to trans-CuEn, Cu nanocubes of 25 nm were loaded onto carbon paper support, as that was the intermediate size of cubic shaped particles (10 ~ 40 nm) in trans-CuEn. Loading amount of Cu nanocubes was based on the mass of Cu loaded for trans-CuEn, with the assumption that all the copper is contained within the cubic structure.

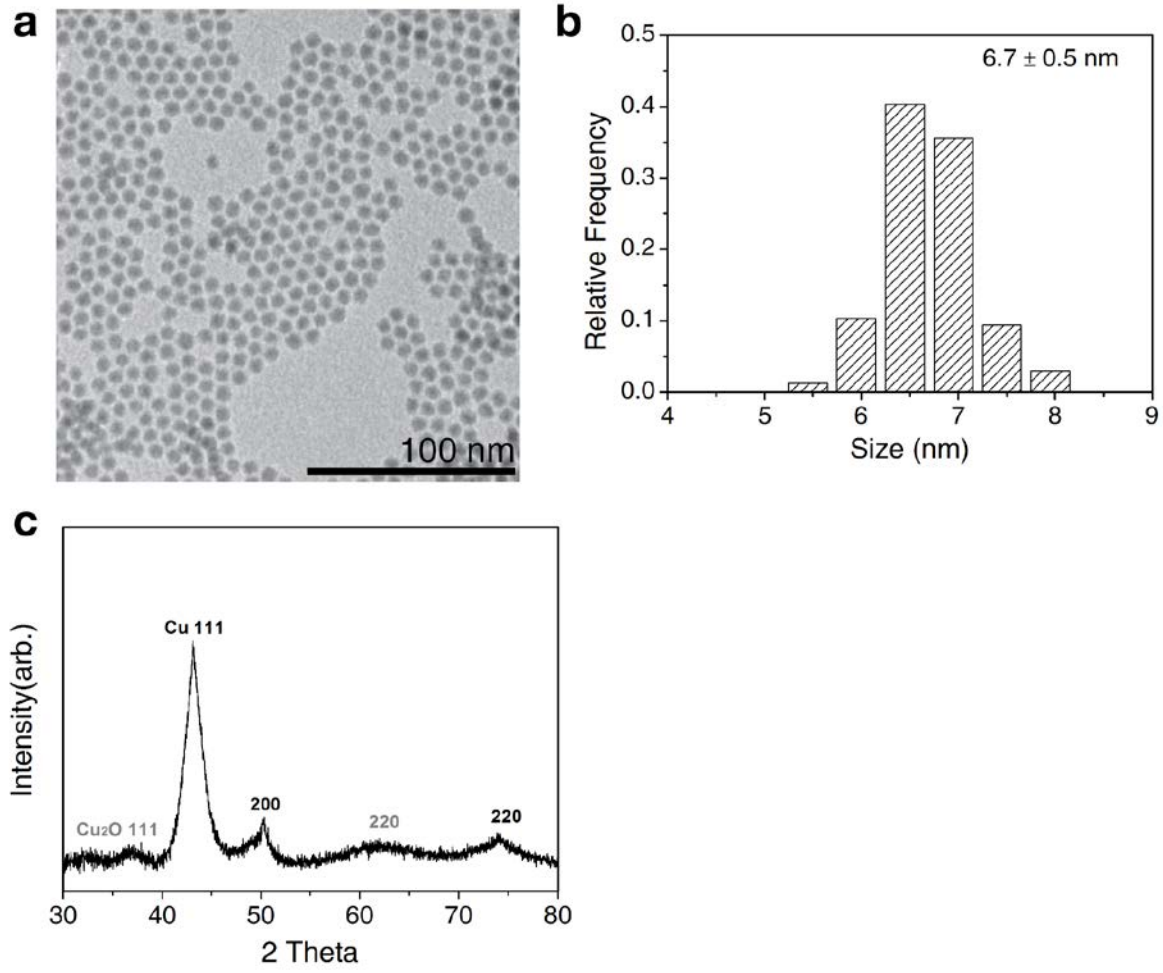

Figure S1. Characterization of Cu nanoparticles. (a) TEM image of Cu nanoparticles. (b) Size distribution of Cu nanoparticles and their average size. (c) XRD of Cu nanoparticles. Due to the tendency of copper to oxidize, Cu nanoparticles contain native oxide layers at their surface even though they are protected by surface ligands.

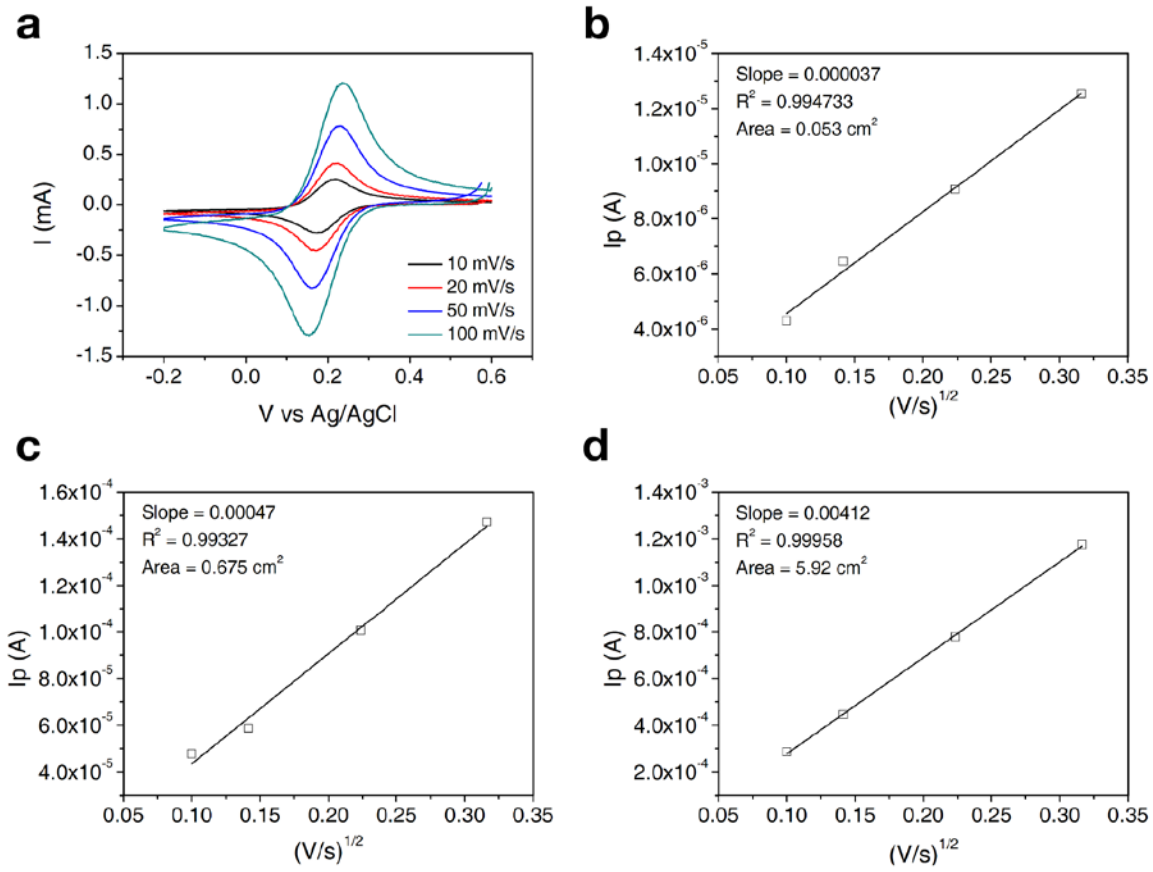

Figure S2. Surface area analysis of carbon supports. (a) Cyclic voltammetry (CV) of carbon paper used in this work under conditions of 1mM ferricyanide in 0.1M KCl solution. Cathodic and anodic peak currents are from the reduction and oxidation of ferricyanide. Peak current versus square root of scan rate for glassy carbon electrode (b) and highly polished graphite plate (c), which have geometric areas 0.07cm^2 and 0.77cm^2, respectively. Area estimated for glassy carbon from the CV analysis is slightly underestimated due to the Teflon sheath preventing effective wetting at the outer edges. However, the results show a close match to their expected areas (~1 cm$^2_{real}$/cm$^2_{geo}$) (d) CV analysis of carbon paper (1cm$^2_{geo}$), which shows that its real surface area is 5.92cm^2. The area determined in this manner was compared with the area estimated from double layer capacitance. With 52.3μF/cm$^2_{real}$ measured from glassy carbon substrate, carbon paper support (1cm$^2_{geo}$) was estimated to exhibit 4.9cm$^2_{real}$ (254μF), which is, though slightly lower, close to the area estimated by charge transfer to ferricyanide.

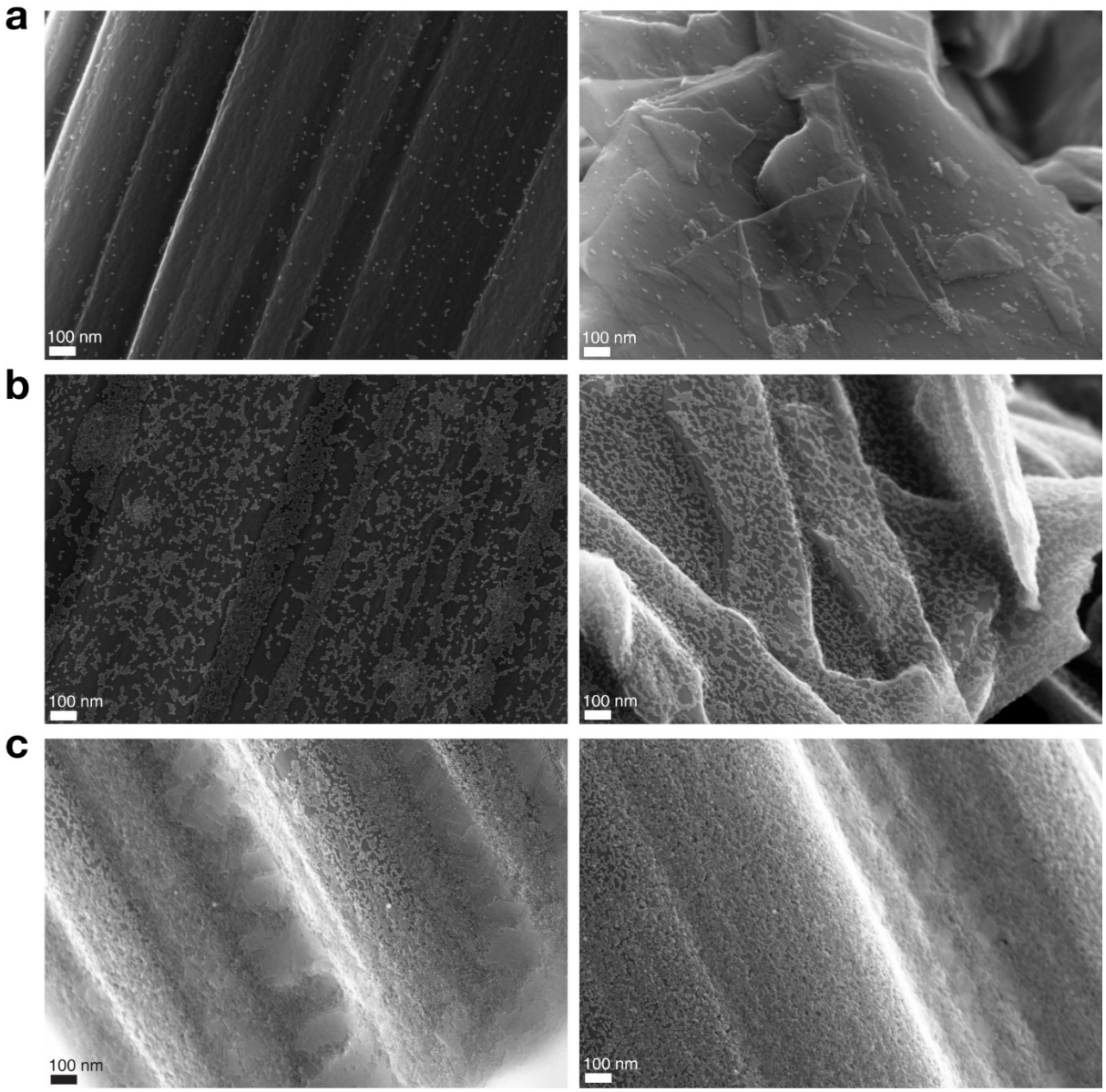

Figure S3. SEM images of Cu NPs on carbon paper support at ×1 (a), ×5 (b), and ×22.5 (c) loading. ×22.5 loading is expected to cover ~2 times the real area provided by carbon paper support ($1cm^2_{geo}$), which is estimated from the average size of the particles. This results in multiple stacked layers of Cu NPs in some parts of the area.

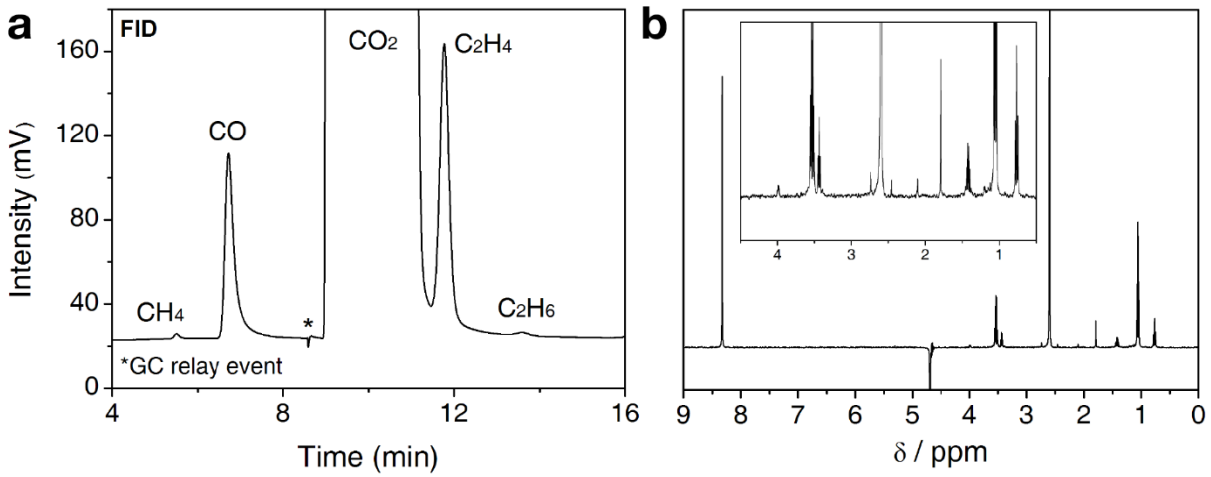

Figure S4. Gas chromatograph (a) and NMR spectrum (b) from ×22.5 loading of Cu NP ensembles tested at -0.81 V vs. RHE. Features shown in (b) at 2.6 ppm and 4.7 ppm are DMSO internal standard and suppressed water peak, respectively.

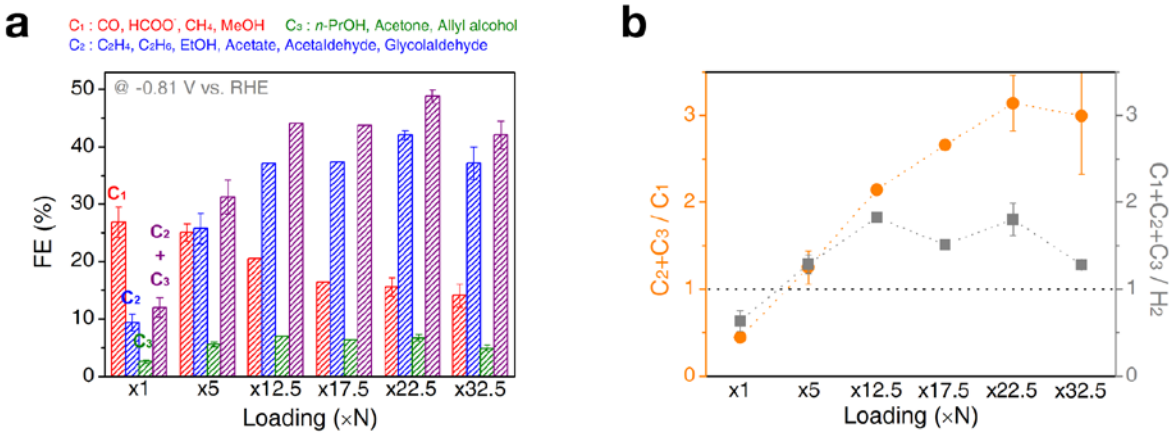

Figure S5. (a) Faradaic efficiencies (FE, %) for C_1, C_2, and C_3 products at various loading conditions. (b) Relative ratio of the FE. Error bars shown are one standard deviation from three independent measurements.

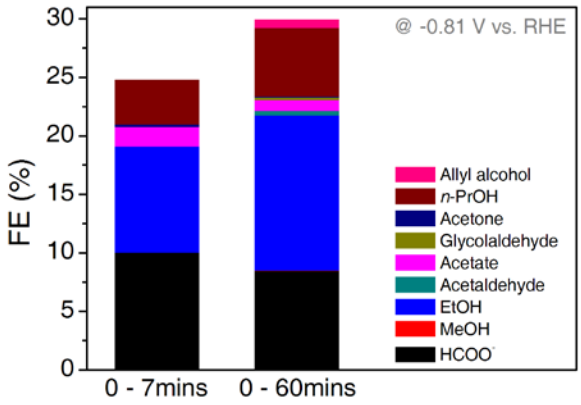

Figure S6. Comparison of liquid products at different time periods for ×22.5 loading condition during electrolysis at -0.81 V vs. RHE.

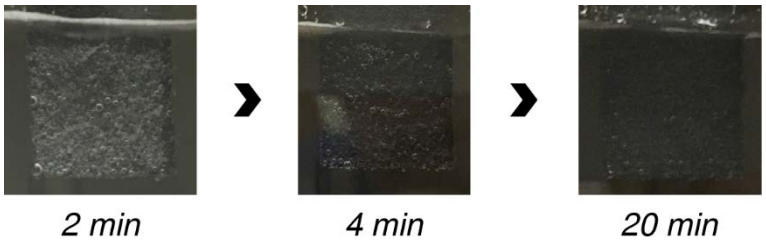

Figure S7. Photographs of the electrode (×22.5 loading condition) during electrolysis at -0.81 V vs. RHE.

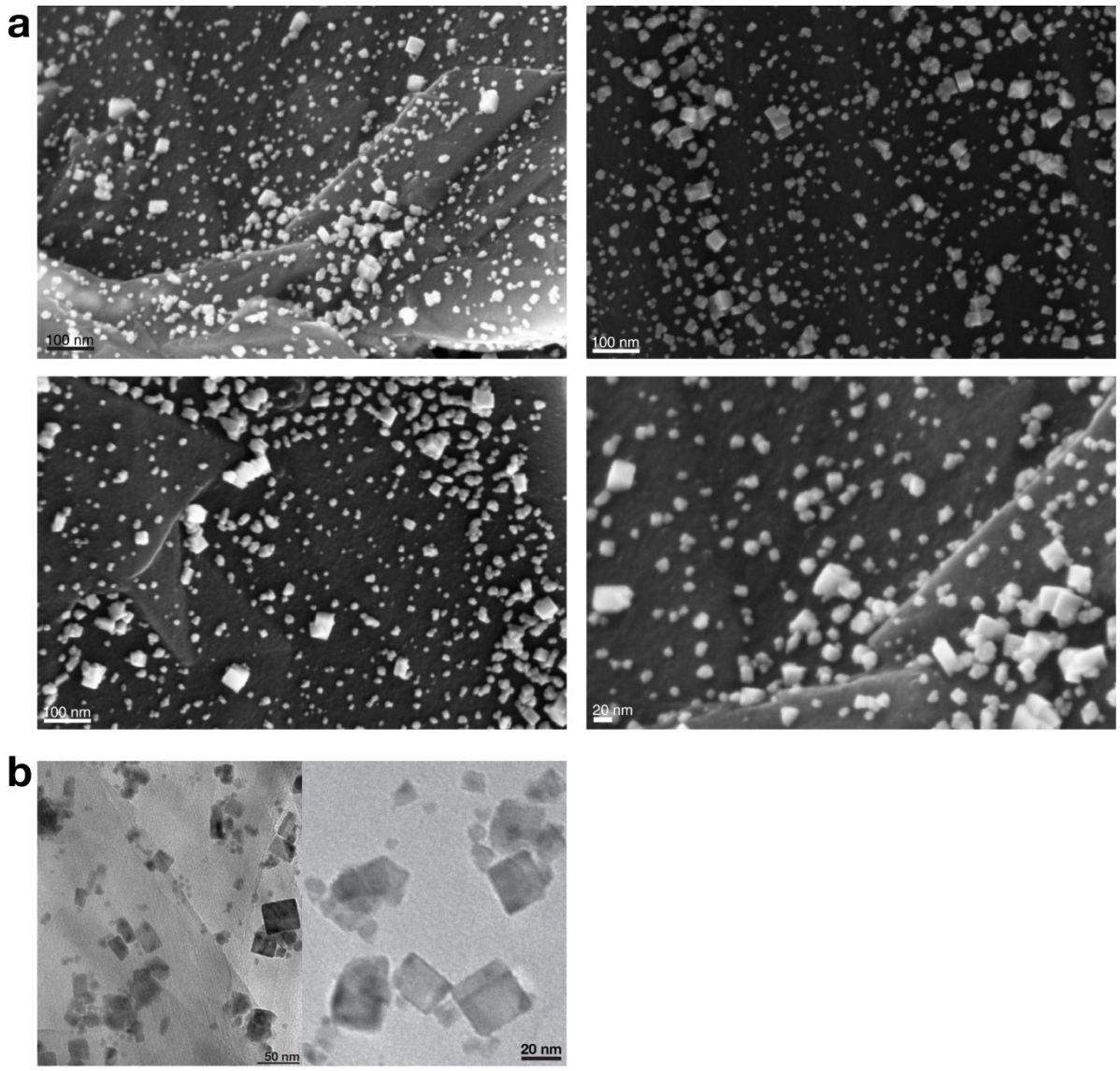

Figure S8. (a) SEM images of Cu NP ensemble (×22.5 loading) on carbon paper support after 1hr electrolysis. (b) TEM images of structurally transformed Cu NP ensemble. Overlaying object shown in the left image is the supporting carbon material.

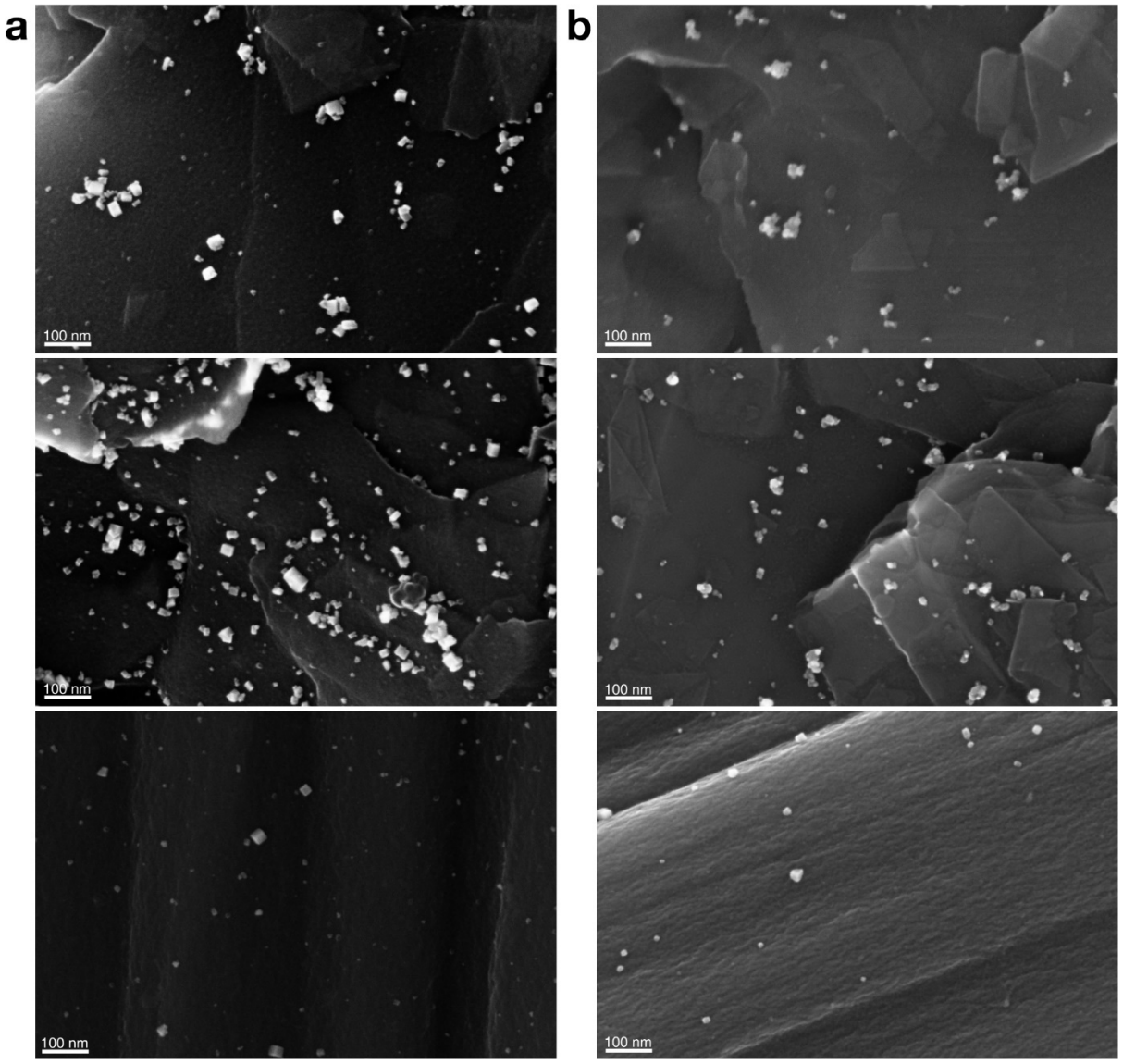

Figure S9. SEM images of ×5 loaded (a) and ×1 loaded (b) carbon paper support after 1hr electrolysis.

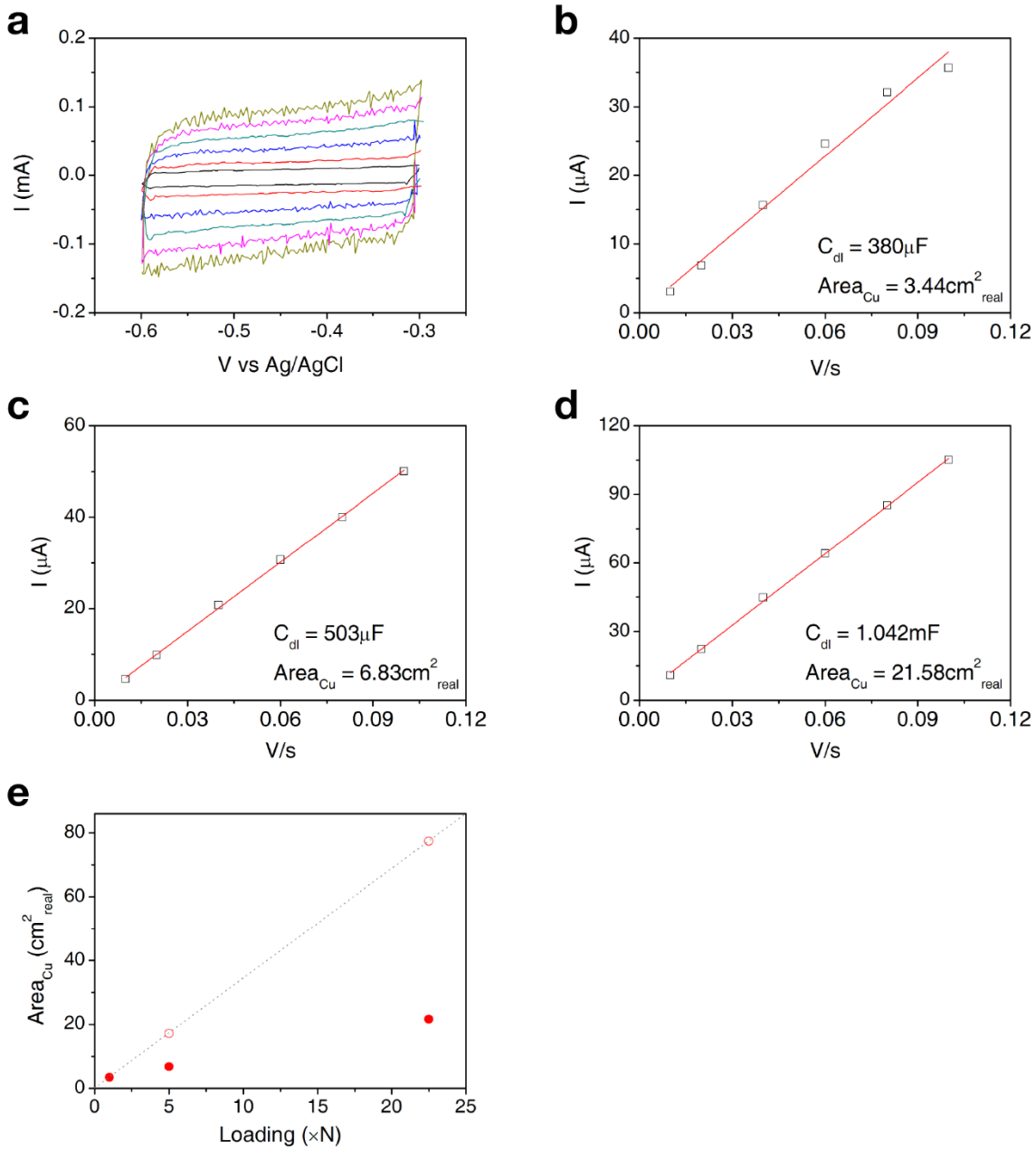

Figure S10. (a) CV curve of ×22.5 loaded carbon paper support after electrolysis in 0.1 M $KHCO_3$ saturated with Ar. Current versus scan rate plots of ×1 loading (b), ×5 loading (c), and ×22.5 loading (d) conditions. Capacitance values shown are before subtraction of bare carbon paper support. (e) Trend of active copper surface area (closed circles) with increased loadings. Open circles show expected surface areas, when area should be increasing in the same manner as the loadings, assuming minimal degree of structural transformation occurring as in the case of ×1 loading.

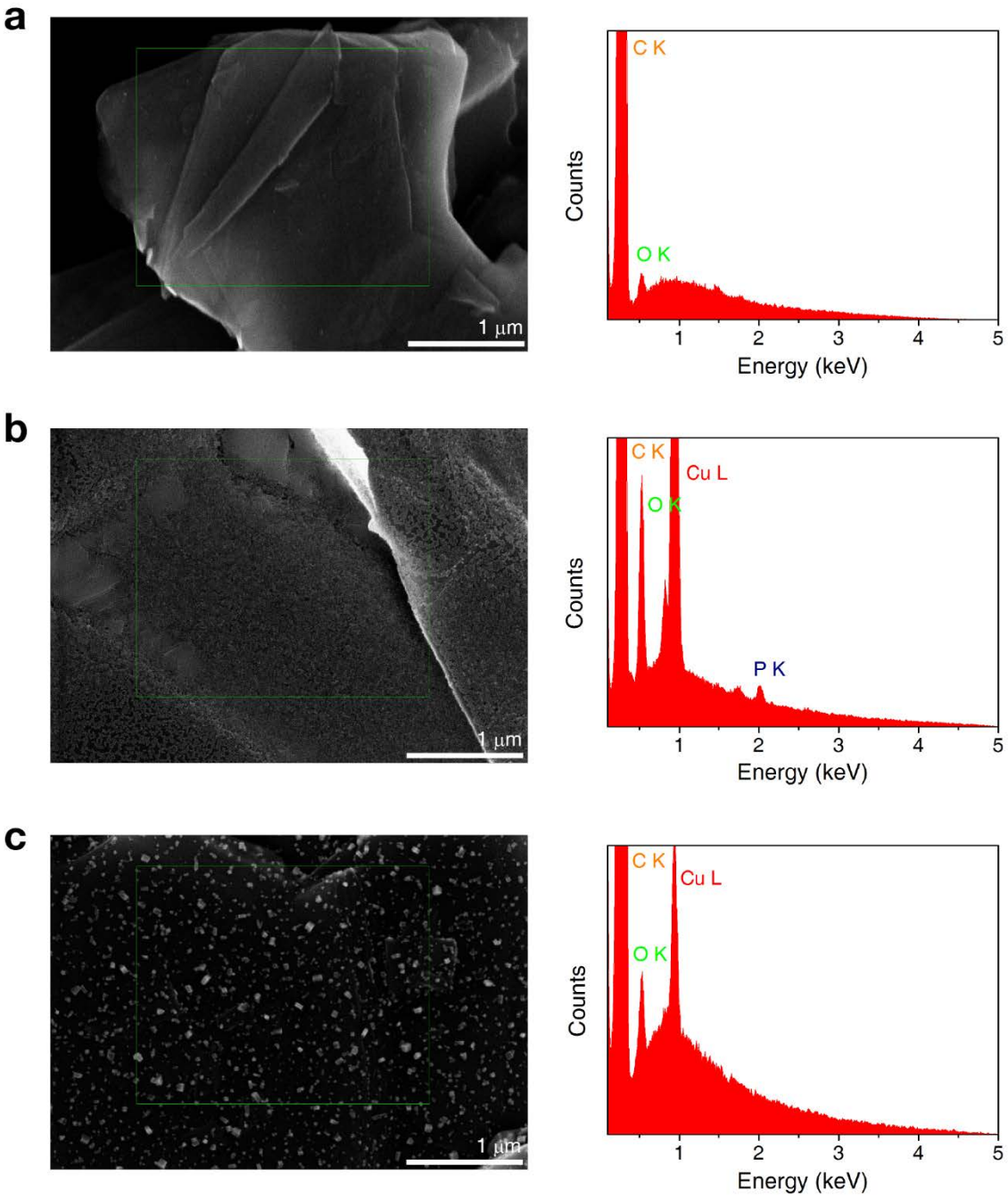

Figure S11. SEM images and EDS spectra (collected from the area specified in the images) of pure carbon support (a) and Cu NP ensembles (×22.5 loading) before (b) and after (c) transformation. Loss of the phosphorus signal (originating from phosphonic acid surface ligands) is observed after structural transformation.

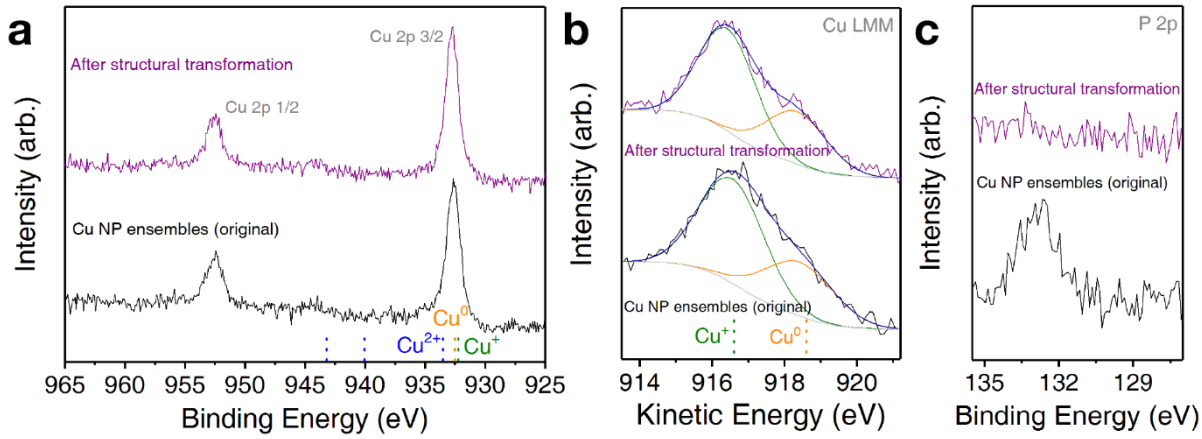

Figure S12. X-ray photoemission spectra for Cu 2p (a), Cu LMM Auger (b) and P 2p (c) of Cu NP ensembles (×22.5 loading) and structurally transformed Cu NP ensembles after 1hr electrolysis. Structurally transformed Cu NP ensembles were transferred under argon right after the end of electrolysis to minimize exposure to air. However, similar extent of surface oxidation to the original Cu NPs was still observed, with both exhibiting Cu^{+}/Cu^{0} ratios of 1.82. Loss of the phosphorus signal is observed after structural transformation.

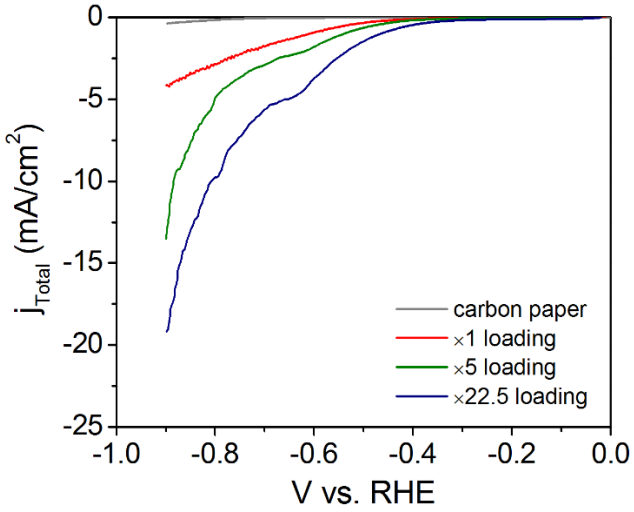

Figure S13. Linear sweep voltammetry (scan rate : 50 mV/s) of carbon paper support compared with structurally transformed Cu NP ensembles at various loading conditions (after 1hr electrolysis).

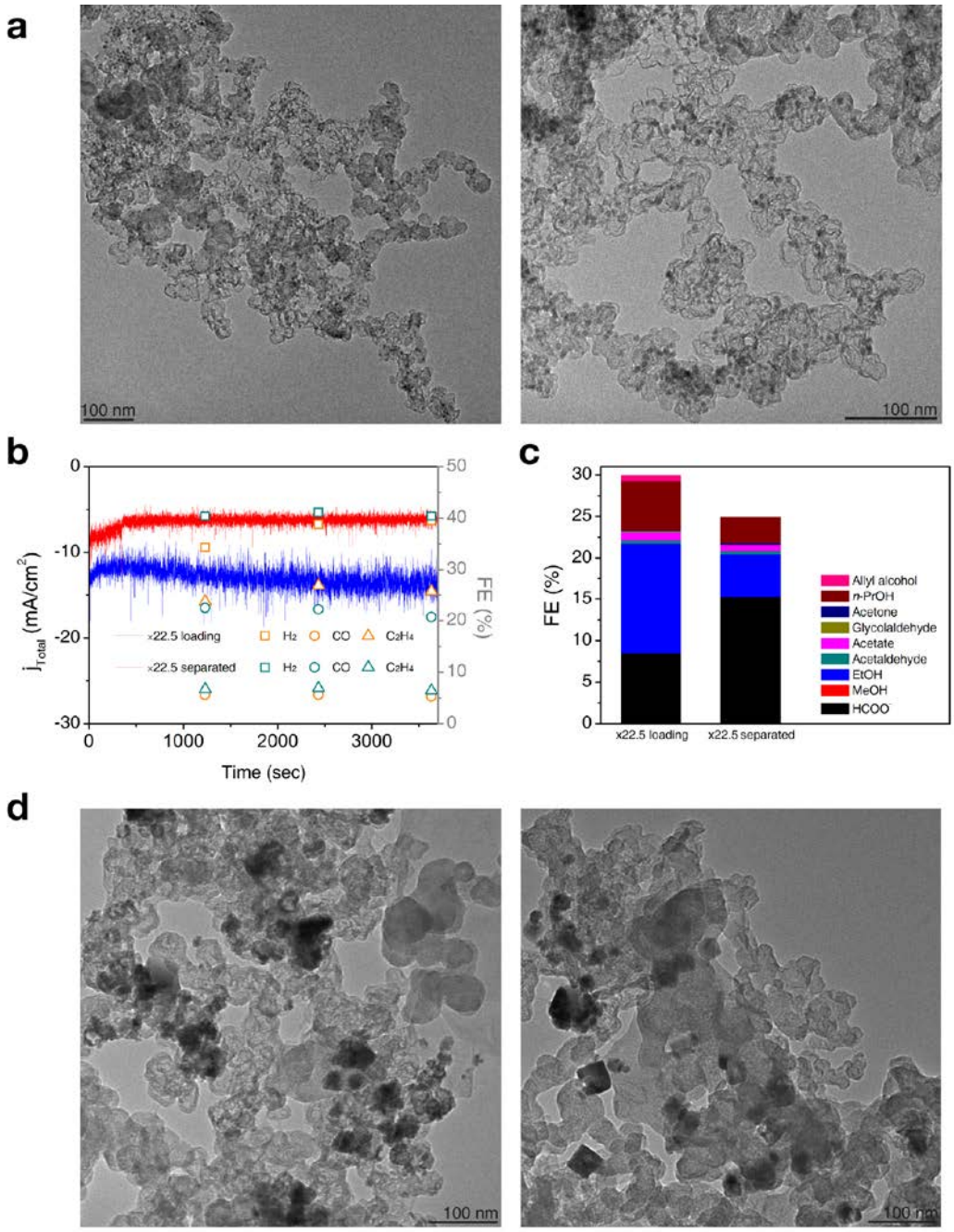

Figure S14. (a) TEM images of Cu NPs (amount identical to ×22.5 loading) separated by mixing with carbon black. (b) Total current density (geometric area based) and FE of major gas products for ×22.5 loading (at -0.81 V vs. RHE) and ×22.5 separated (at -0.84 V vs. RHE). FE of CH_4 and C_2H_6 are omitted. (c) FE of liquid products for ×22.5 loading and ×22.5 separated. (d) TEM images of ×22.5 separated Cu NPs after electrolysis. Randomly aggregated nanoparticles are observed together with few cubic shaped structures.

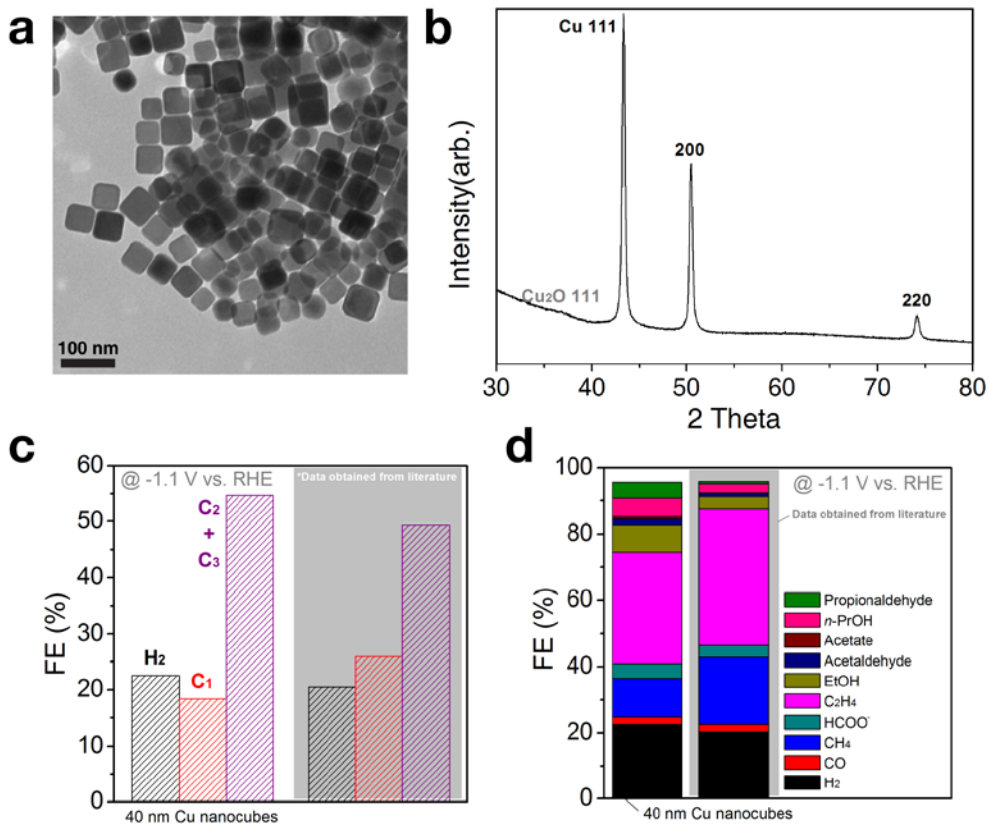

Figure S15. (a) TEM images of Cu nanocubes with 40 nm average edge length. (b) XRD of Cu nanocubes. (c) Activity measured from 40 nm nanocubes under identical procedures to the previous report (1) showing similar selectivity to multi-carbon products at -1.1 V vs. RHE. Column graph on the right is from the data provided in ref. 1 (d) FE of the individual products measured and compared to the values from the previous report. Data from ref. 1

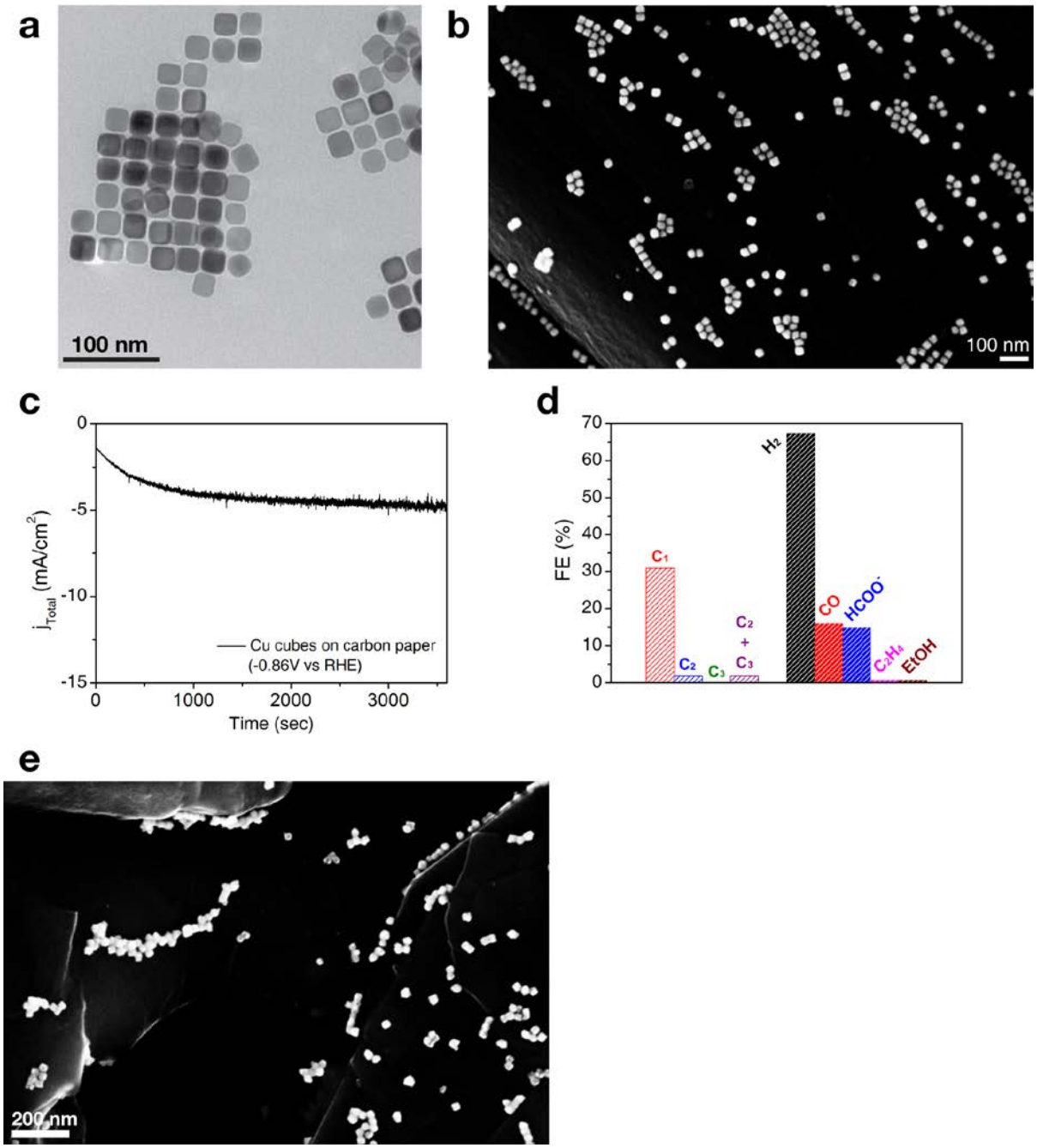

Figure S16. (a) TEM image of Cu nanocubes (25 nm in size). (b) SEM image of Cu nanocubes loaded onto carbon paper support at same mass loadings to trans-CuEn (47.7 μg of copper). (c) Total current density of Cu cubes loaded onto carbon paper support at -0.86 V vs. RHE. (d) FE of C_1, C_2, C_3 and major products generated. (e) SEM image of Cu nanocubes after electrolysis.

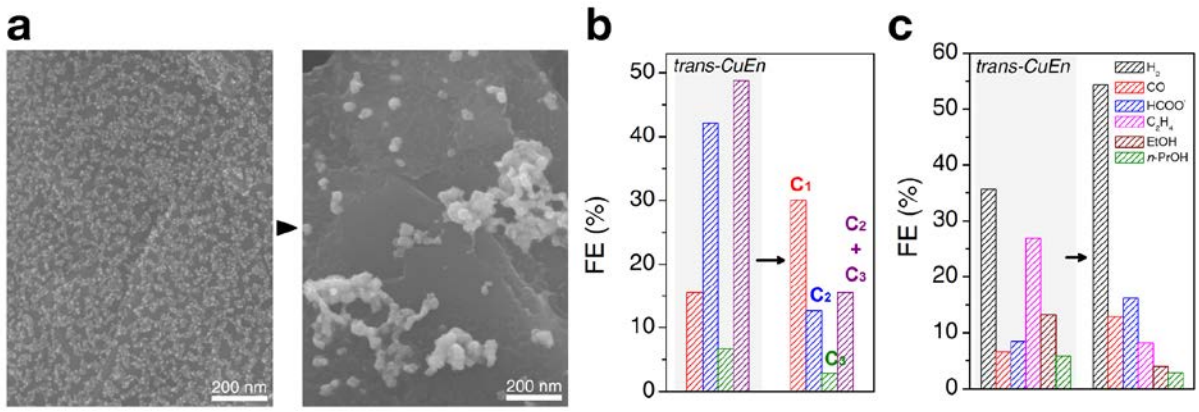

Figure S17. (a) SEM image of Cu NP ensembles (×22.5 loading, condition identical to trans-CuEn) treated with Ar plasma (Left). Ar plasma treated NPs lose their individual shape and coalesce with neighboring NPs. Plasma treated NPs after electrolysis at -0.84 V vs. RHE (Right) exhibit very large irregular structures, in contrast to what are observed in trans-CuEn. FEs of C_1, C_2, C_3 (b) and major products (c) generated from the plasma treated catalyst (at -0.84 V vs. RHE) compared to those of trans-CuEn (shaded in gray). This shows that simply having identical amount of Cu with similar coverage on a carbon support doesn`t lead to the unique structures and catalytic performance of trans-CuEn.

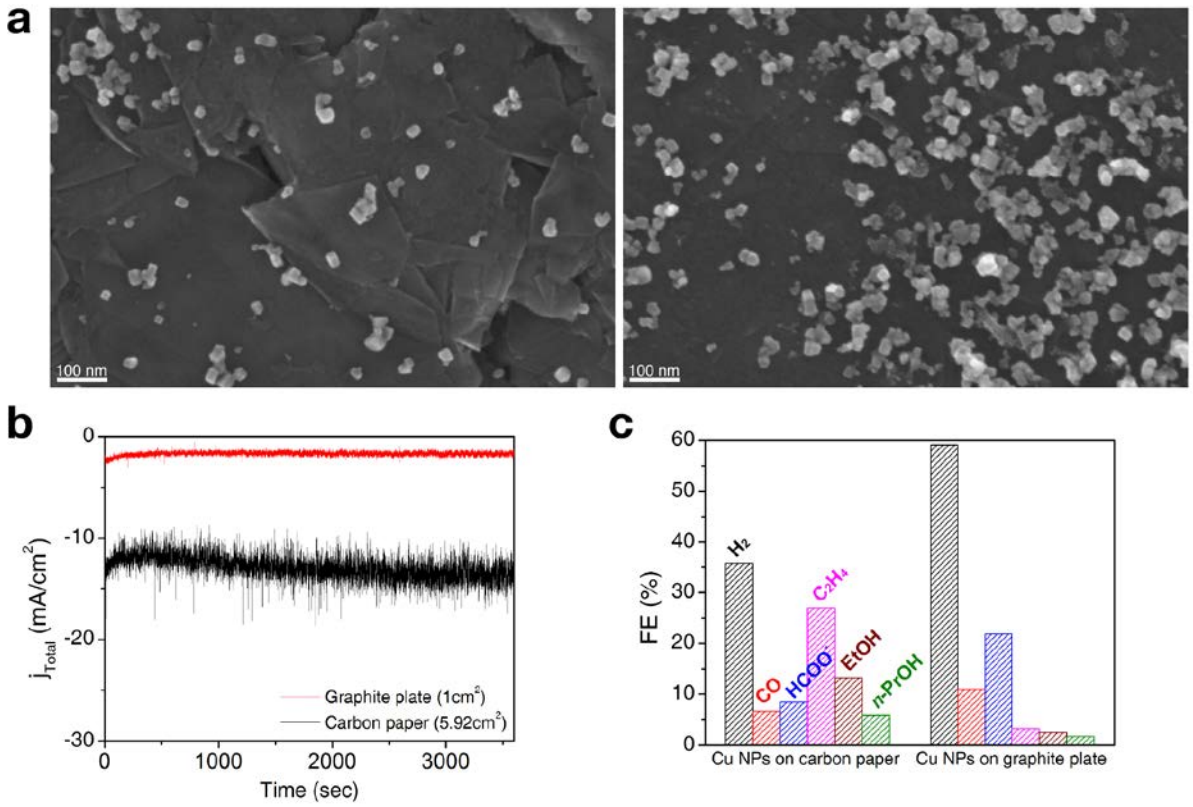

Figure S18. (a) SEM images of Cu NP ensembles (density identical to trans-CuEn) on polished graphite electrode after electrolysis. (b) Total current density (geometric area based) of Cu NPs on graphite plate ($1cm^2_{real}$), with identical loading density to trans-CuEn, compared with that of trans-CuEn at -0.81 V vs. RHE. (c) FE of major products compared for two different configurations.

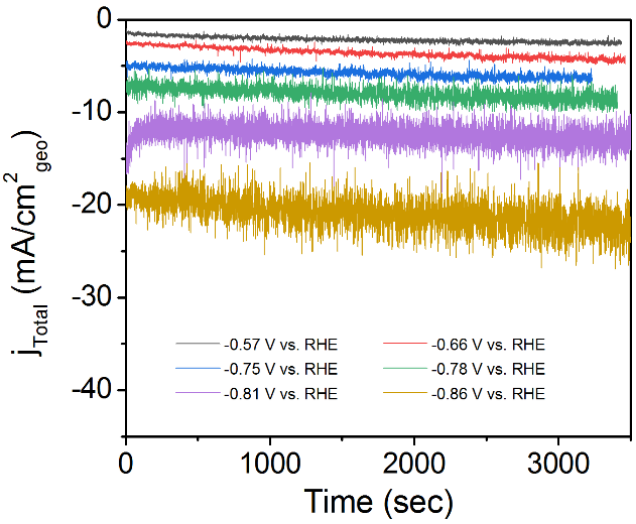

Figure S19. Steady-state current densities of trans-CuEn at various potentials in 0.1 M $KHCO_3$.

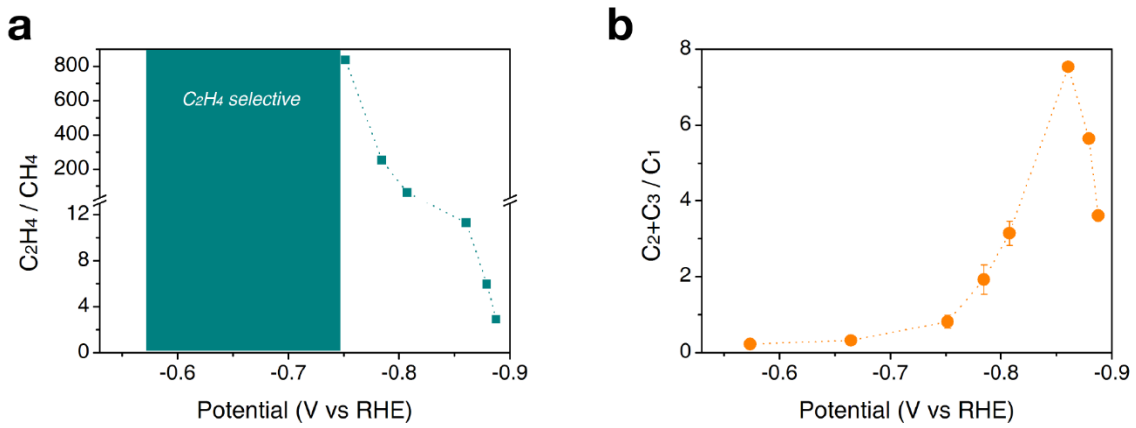

Figure S20. (a) C_2H_4/CH_4 ratio at various potentials for trans-CuEn. The region labeled as 'C_2H_4 selective' is the region where only C_2H_4 is observed without CH_4. (b) C_2+C_3/C_1 at various potentials for trans-CuEn. The charge consumed at the catalyst for C_2-C_3 product formation becomes 88% of the total charge passed for CO_2 reduction (excluding H_2 evolution) at -0.86 V vs. RHE.

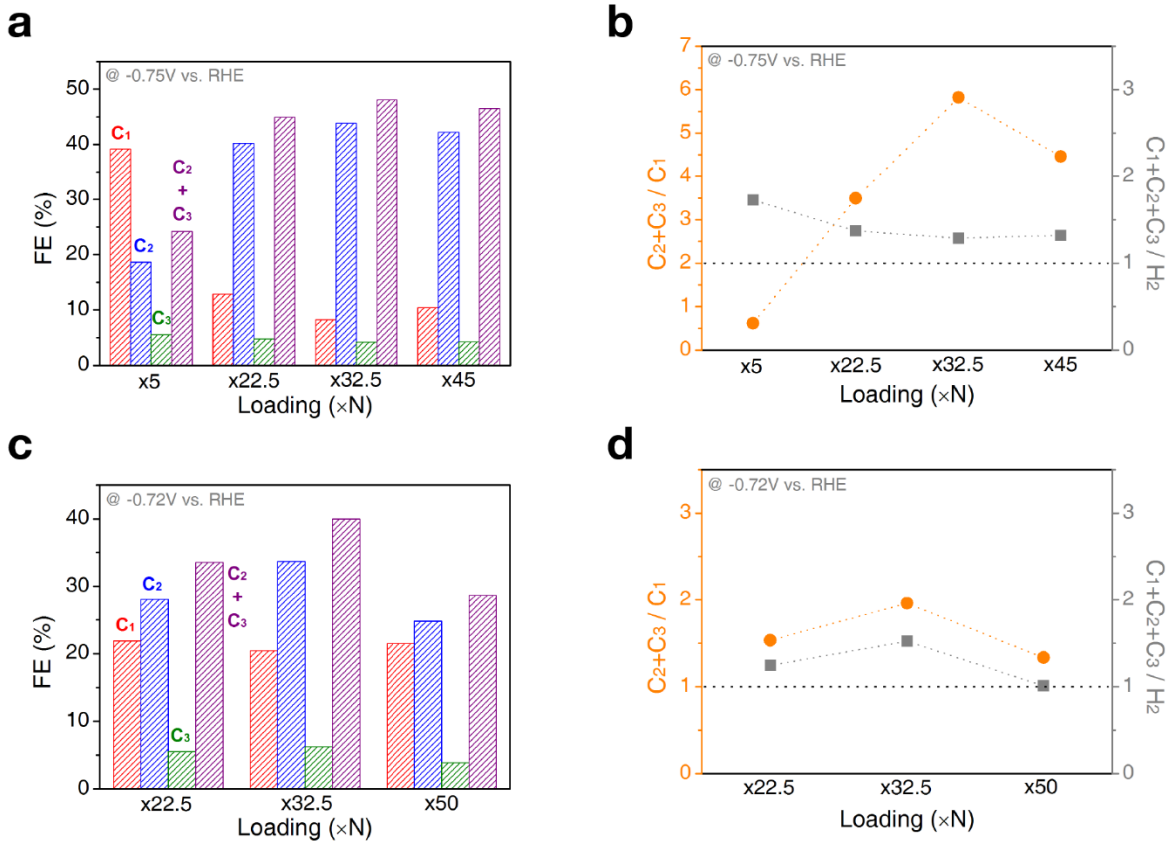

Figure S21. Faradaic efficiencies (FE, %) for C_1, C_2, and C_3 products (a, c) and relative ratio of the FE (b, d) at various loading conditions in 0.1M $CsHCO_3$ at 1 atm CO_2.

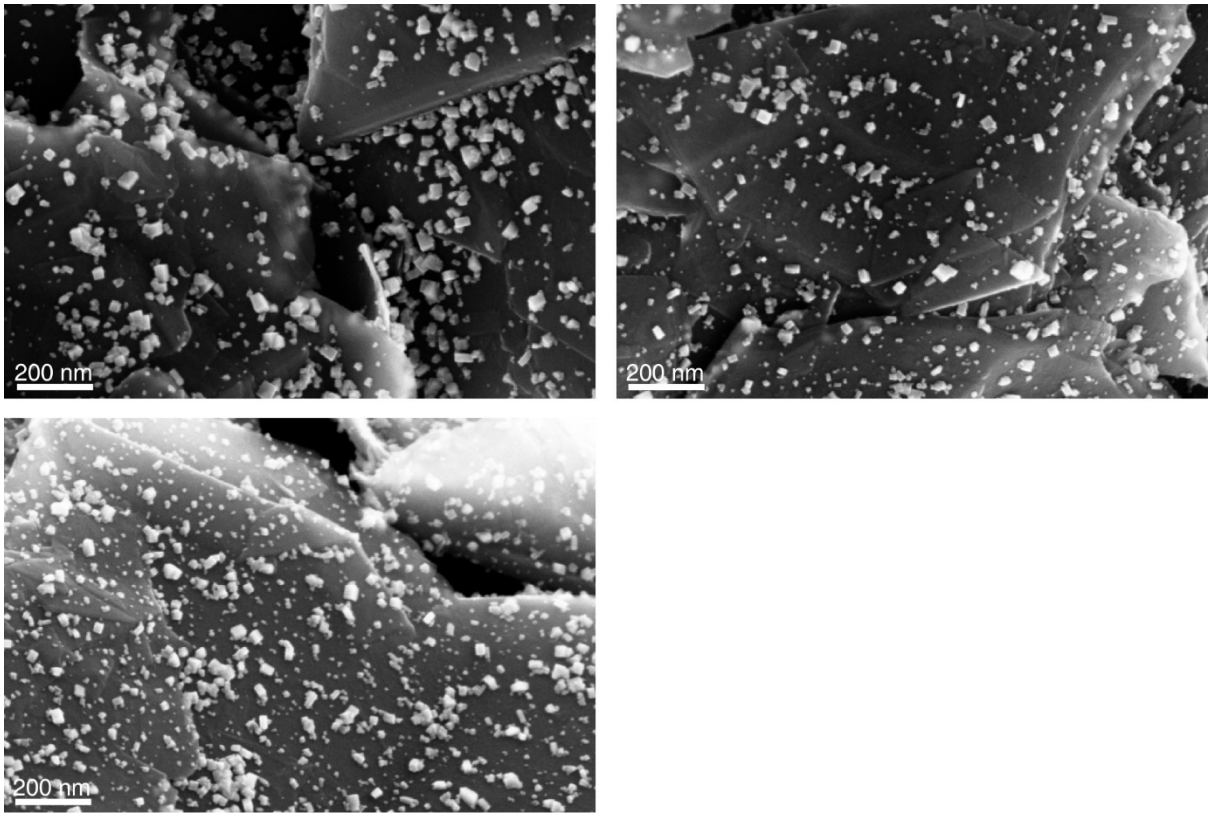

Figure S22. Structural transformation observed of Cu NP ensembles (×32.5 loading) after electrolysis in 0.1M $CsHCO_3$ at -0.75 V vs. RHE.

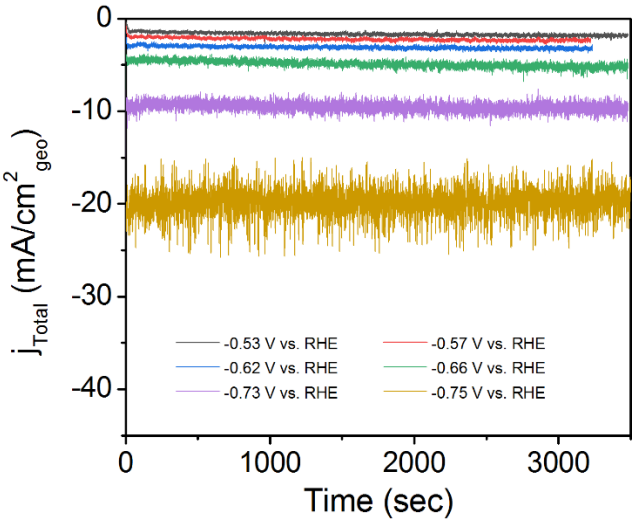

Figure S23. Steady-state current densities of trans-CuEn 2 at various potentials in 0.1 M $CsHCO_3$.

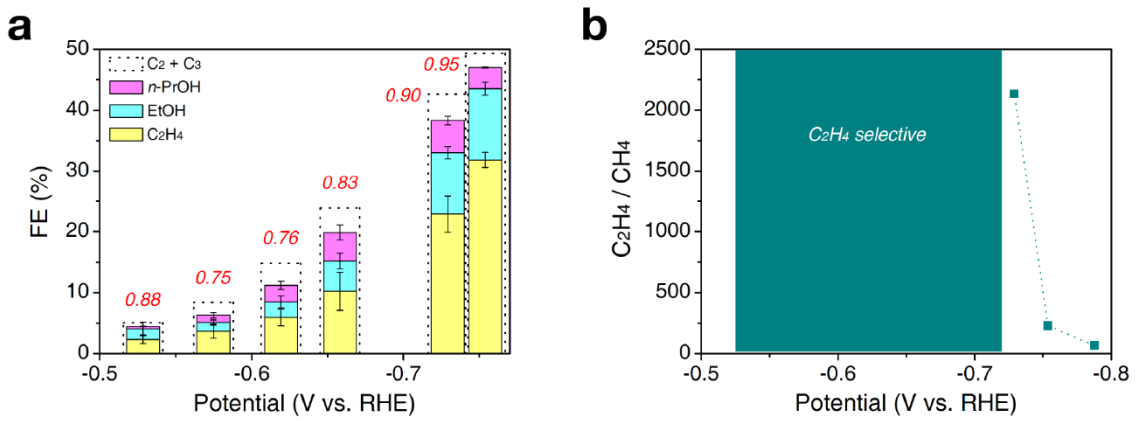

Figure S24. (a) Ethylene, ethanol, and *n*-propanol FE with the dotted line showing the overall C_2-C_3 FE at various potentials for trans-CuEn 2 in 0.1 M $CsHCO_3$. Numbers in red are the fraction of sum of ethylene, ethanol, and *n*-propanol out of total C_2-C_3 products. (b) C_2H_4/CH_4 ratio at various potentials for trans-CuEn 2 in 0.1 M $CsHCO_3$. The region labeled as 'C_2H_4 selective' is the region where only C_2H_4 is observed without CH_4.

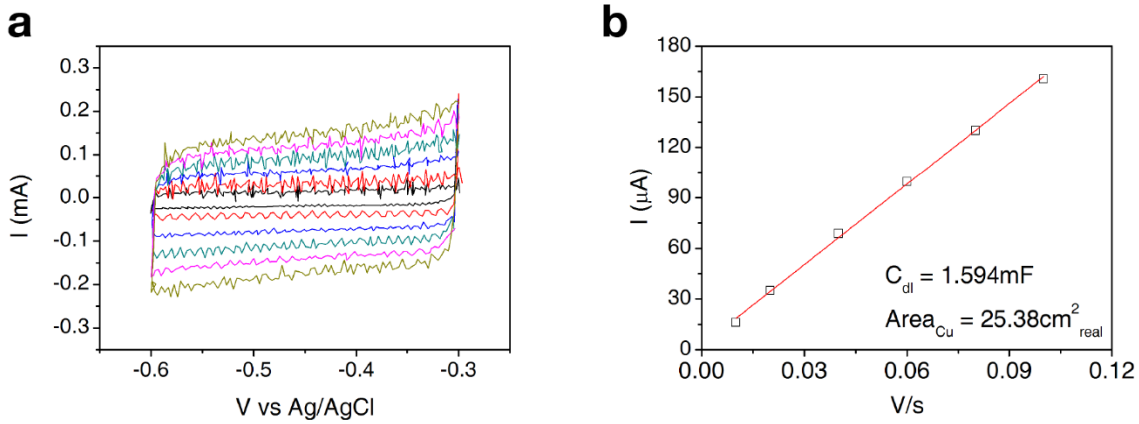

Figure S25. (a) CV curve of trans-CuEn 2 after electrolysis in 0.1 M $CsHCO_3$ saturated with Ar. (b) Current versus scan rate plot. Capacitance value shown is before subtraction of the carbon paper support.

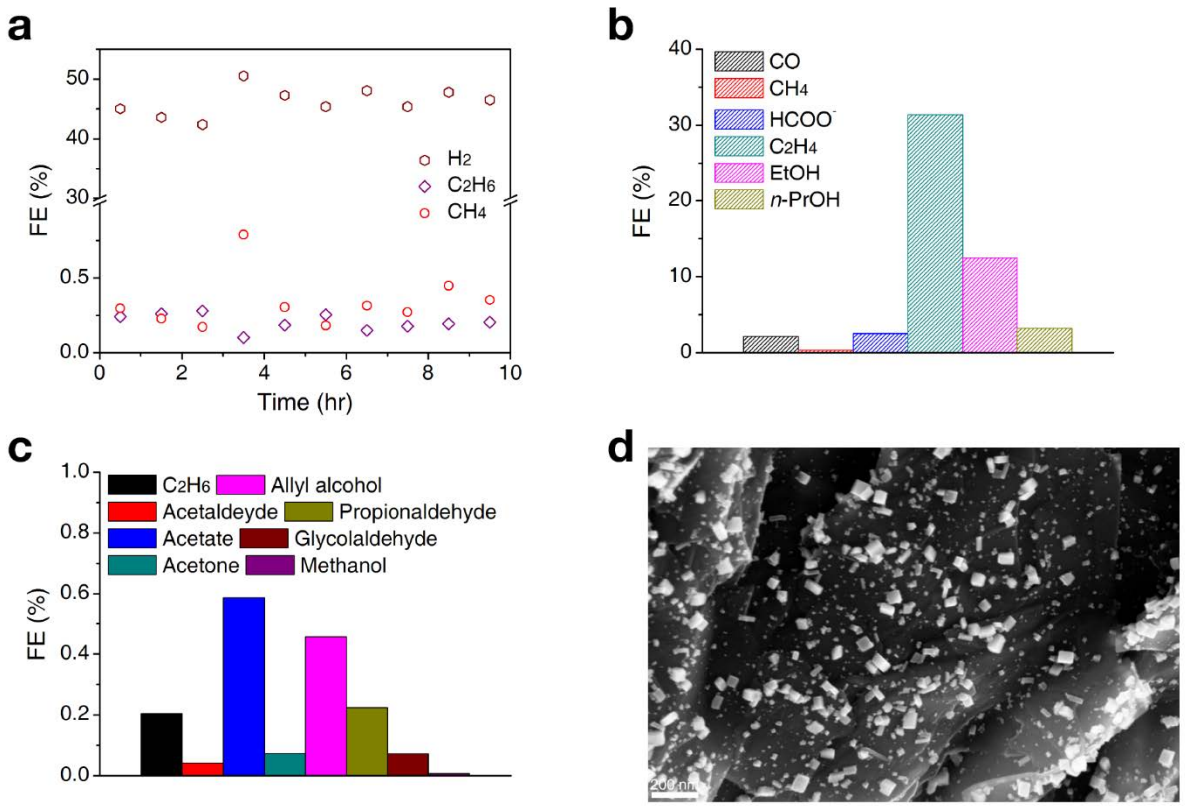

Figure S26. (a) FE of other gas products measured every hour during extended period (10 hr) of electrolysis. (b) Average FE of major products during extended period of electrolysis. (c) Average FE of minor products during extended period of electrolysis. (d) SEM image of trans-CuEn 2 after 10 hr of electrolysis.

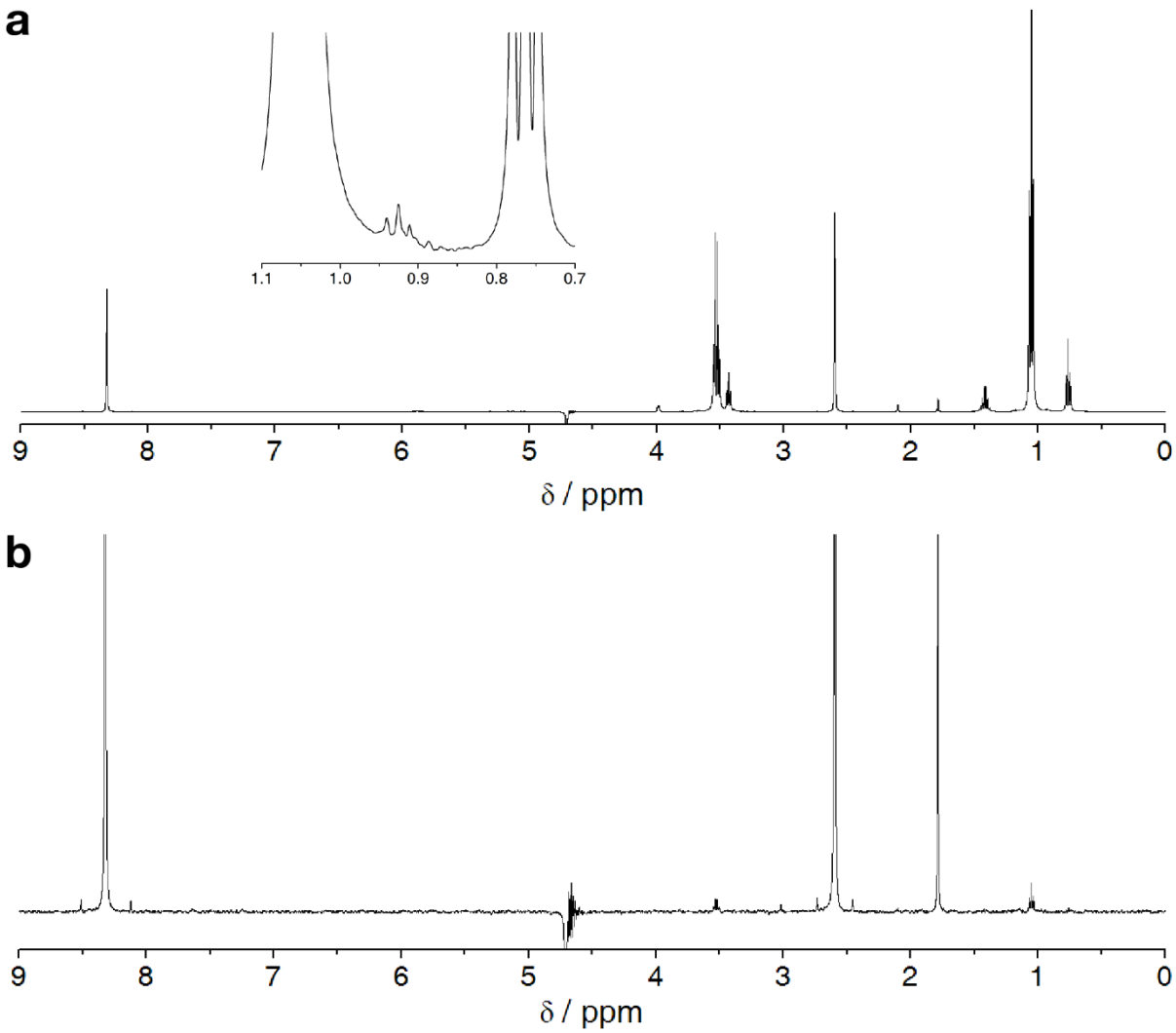

Figure S27. NMR spectra collected from 10 hr electrolysis of trans-CuEn 2 at -0.75 V vs. RHE in 0.1 M $CsHCO_3$. Liquid products are analyzed from both the working electrode compartment (a) and the counter electrode compartment (b). A triplet at 0.92 ppm from propionaldehyde is observed. A singlet at 9.57 ppm was found as well. However, quartet (2.44 ppm) that should be present overlapped with satellites of DMSO. Liquid extracted from the counter electrode compartment contains small amounts of formate, acetate, ethanol, and -*n*-propanol. This is due to liquid products (mainly the ones bearing negative charge) crossing the anion exchange membrane to the counter electrode chamber. Features shown at 2.6 ppm and 4.7 ppm are DMSO internal standard and suppressed water peak, respectively.

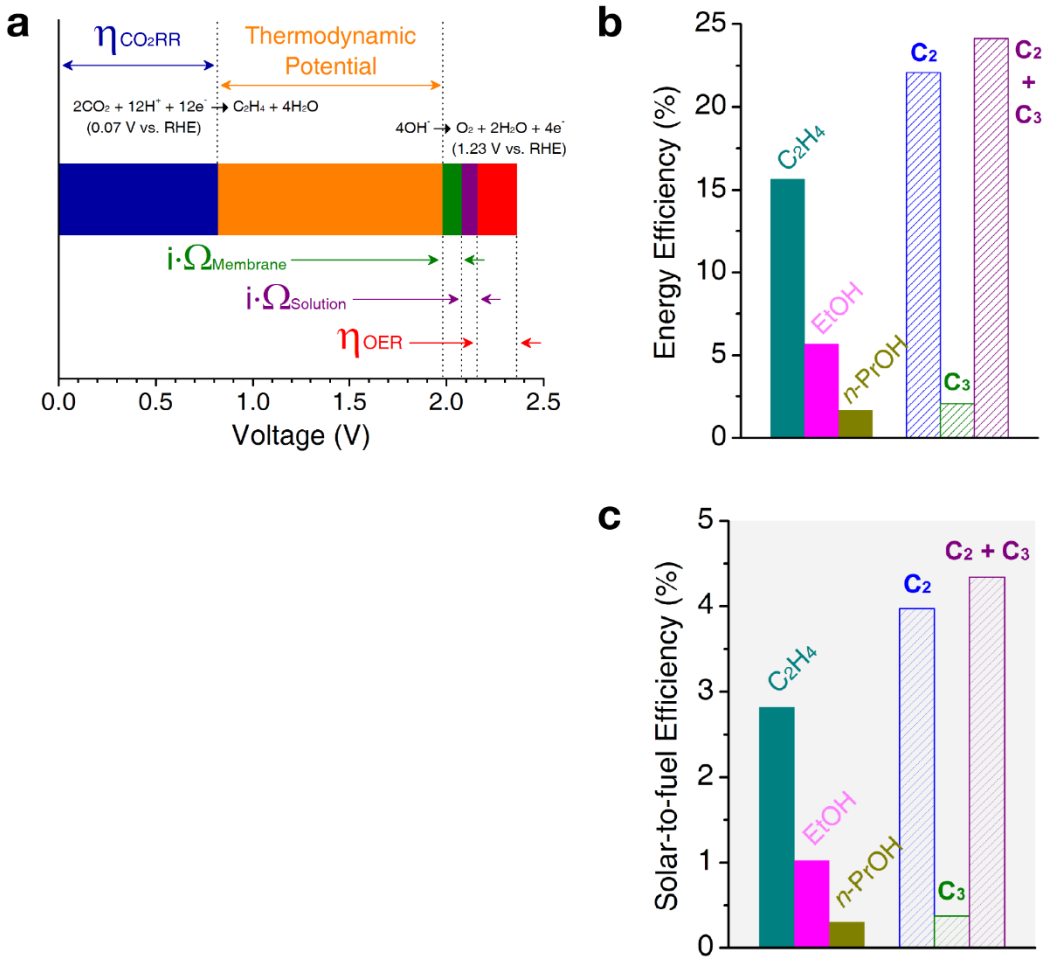

Figure S28. (a) Voltage distributions (2.36 V applied) in an electrolyzer incorporating NiFe hydroxide anode and bipolar membrane. Overpotential at the anode (η_{OER}) and voltage losses from the solution and the membrane are from ref. 2, which describes a system operating at ~16 mA (close to the operating condition of the catalyst described in this work at -0.75 V vs. RHE). Overpotential at the cathode (η_{CO2RR}) shown is for ethylene and it will vary depending on the product (Table S9). (b) Energy efficiency estimated for major C_2-C_3 products. (c) Solar-to-fuel efficiency estimated for major C_2-C_3 products, assuming 18% solar-to-electricity efficiency provided from commercial Si solar cells.

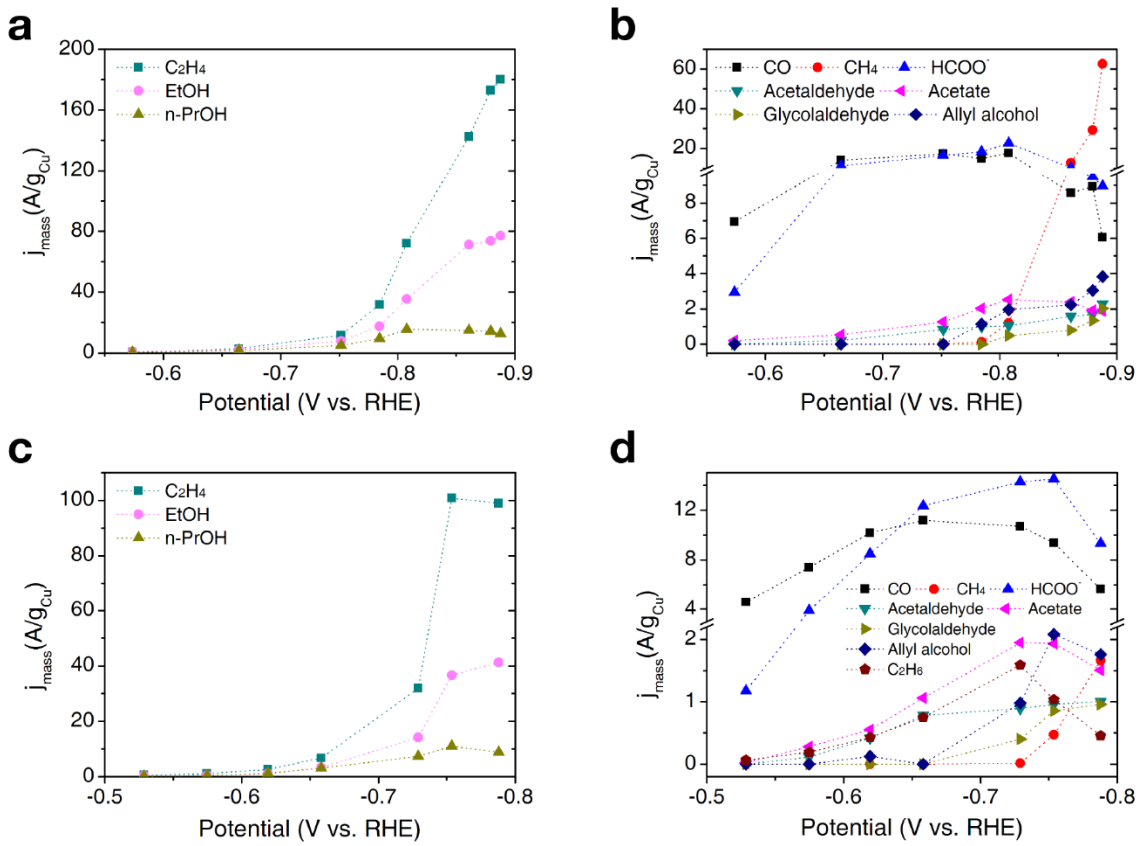

Figure S29. Mass activities of trans-CuEn measured in 0.1 M $KHCO_3$ for major (a) and minor (b) products. Mass activities of trans-CuEn 2 measured in 0.1 M $CsHCO_3$ for major (c) and minor (d) products.

Table S1. Loading conditions of Cu nanoparticles on carbon paper support.

×N	**Mass (μg)**	**# of NPs**	**NPs/cm$^2_{real}$**
×1	2.12 μg	1.49×10^{12}	2.52×10^{11}
×5	10.6 μg	7.45×10^{12}	1.26×10^{12}
×12.5	26.5 μg	1.86×10^{13}	3.15×10^{12}
×17.5	36 μg	2.61×10^{13}	4.41×10^{12}
×22.5	47.7 μg	3.35×10^{13}	5.66×10^{12}
×32.5	68.9 μg	4.84×10^{13}	8.18×10^{12}

Table S2. Faradaic efficiencies (%) of CO_2 reduction products at various loading conditions in 0.1 M $KHCO_3$ at 1 atm CO_2.

Products	**×1 loading (-0.87 V vs. RHE / 2.6 mA/cm$^2_{geo}$)**	**×5 loading (-0.85 V vs. RHE / 5.0 mA/cm$^2_{geo}$)**	**×22.5 loading (-0.81 V vs. RHE / 12.7 mA/cm$^2_{geo}$)**
CO	10.5%	11.5%	6.6%
CH_4	1.1%	0.5%	0.4%
$HCOO^-$	15.1%	13.0%	8.5%
MeOH	*trace*	-	*trace*
C_2H_4	4.6%	15.1%	27.0%
C_2H_6	-	0.1%	0.3%
EtOH	3.8%	8.9%	13.3%
Acetaldehyde	0.3%	0.5%	0.4%
Acetate	0.8%	1.0%	0.9%
Glycolaldehyde	-	-	0.2%
Acetone	-	0.2%	0.1%
n-PrOH	2.4%	5.2%	5.9%
Allyl alcohol	0.2%	0.2%	0.7%

Table S3. Onset potentials for C_2-C_3 products compared against pristine copper foil.

	Electrolyte	**Potential (V vs. RHE)**	**C_2-C_3 product FE (%)**	**Ref.**
trans-CuEn	0.1M $KHCO_3$	-0.57 V	C_2H_4 1.1%, EtOH 1.9%, *n*-PrOH 1.1%	This work
trans-CuEn 2	0.1M $CsHCO_3$	-0.53 V	C_2H_4 2.3%, EtOH 1.7%, *n*-PrOH 0.4%	This work
Cu foil	0.1M $KHCO_3$	-0.75 V -0.96 V	C_2H_4 0.4% C_2H_4 10.2%, EtOH 2.5%, *n*-PrOH 2.7%	Ref. 3

Table S4. Faradaic efficiencies of various products observed for trans-CuEn in 0.1 M $KHCO_3$ at 1 atm CO_2.

	-0.57 V / 2.2 mA/cm$^2_{geo}$	**-0.66 V / 3.7 mA/cm$^2_{geo}$**	**-0.75 V / 5.8 mA/cm$^2_{geo}$**	**-0.78 V / 7.8 mA/cm$^2_{geo}$**	**-0.81 V / 12.8 mA/cm$^2_{geo}$**	**-0.86 V / 20.4 mA/cm$^2_{geo}$**	**-0.89 V / 28.5 mA/cm$^2_{geo}$**
C_1	21.6 %	32.8 %	27.9 %	20.4 %	15.5 %	7.3 %	13.0 %
CO	15.2 %	18.2 %	14.3 %	9.1 %	6.6 %	2.0 %	1.0 %
CH_4	-	-	*trace*	0.1 %	0.4 %	2.9 %	10.5 %
$HCOO^-$	6.4 %	14.6 %	13.6 %	11.2 %	8.5 %	2.4 %	1.5 %
MeOH	-	-	-	*trace*	*trace*	*trace*	*trace*
C_2	3.7 %	8.4 %	18.5 %	32.6 %	42.1 %	51.0 %	44.0 %
C_2H_4	1.1 %	3.8 %	9.7 %	19.4 %	27.0 %	33.2 %	30.1 %
C_2H_6	0.2 %	0.6 %	0.5 %	0.7 %	0.3 %	0.1 %	*trace*
EtOH	1.9 %	3.0 %	6.6 %	10.7 %	13.3 %	16.6 %	12.9 %
Acetaldehyde	-	0.3 %	0.7 %	0.6 %	0.4 %	0.4 %	0.4 %
Acetate	0.5 %	0.7 %	1.0 %	1.2 %	0.9 %	0.6 %	0.3 %
Glycolaldehyde	-	-	-	-	0.2 %	0.2 %	0.3 %
C_3	1.1 %	2.1 %	4.2 %	6.6 %	6.7 %	4.1 %	2.8 %
Acetone	-	*trace*	0.1 %	0.1 %	0.1 %	0.1 %	0.1%
n-PrOH	1.1 %	2.1 %	4.1 %	5.8 %	5.9 %	3.5 %	2.1 %
Allyl alcohol	-	-	-	0.7 %	0.7 %	0.5 %	0.6 %
H_2	73.6 %	56.7 %	49.3 %	40.4 %	35.7 %	37.5 %	40.2 %

Table S5. Comparison of C_2-C_3 product formation from various Cu-based heterogeneous catalysts in neutral pH aqueous media at similar applied bias.

	Electrolyte	V (vs. RHE) / j_{Total} (mA/cm^2)	C_2-C_3 product FE (%)	Ref.
trans-CuEn	0.1M $KHCO_3$	-0.86 V / 20.4 mA/cm^2	C_2-C_3 products 55.2% C_2H_4 33.2%, EtOH 16.6%, *n*-PrOH 3.5%	This work
trans-CuEn 2	0.1M $CsHCO_3$	-0.75 V / 21.7 mA/cm^2	C_2-C_3 products 49.3% C_2H_4 31.9%, EtOH 11.7%, *n*-PrOH 3.5%	This work
Cu foil	0.1M $KHCO_3$	-0.89 V / 1.2 mA/cm^2	C_2H_4 3.6%	Ref. 3
Cu_2O derived Cu with $PdCl_2$	0.1M $KHCO_3$	-0.8 V / 7.4 mA/cm^2 -0.9 V / 18.5 mA/cm^2	C_2H_4 5.1%, C_2H_6 10.3%, EtOH 0.9%, *n*-PrOH 2.8% C_2H_4 6.1%, C_2H_6 16.6%, EtOH 8.1%, *n*-PrOH 6.1%	Ref. 5
Electrodeposited Cu_2O on carbon	0.5M $KHCO_3$	-0.93 V / 3.6 mA/cm^2	C_2H_4 10.1%	Ref. 6
Cu mesocrystals (from CuCl film)	0.1M $KHCO_3$	-0.89 V / n/a	C_2H_4 17.1%	Ref. 7
Cu_2O-Cu (Cl induced)	0.1M KCl	-0.8 V / 1.2 mA/cm^2 -1.0 V / 2.7 mA/cm^2	C_2H_4 5%, C_2H_6 0.5% C_2H_4 12%, C_2H_6 3.8%, EtOH 1.5%	Ref. 8
Oxide-derived Cu-foam	0.5M $NaHCO_3$	-0.8 V / 10.9 mA/cm^2	C_2 products 55% C_2H_4 20%, C_2H_6 35%,	Ref. 9
Nanostructured polycrystalline Cu (KF cycled)	0.1M $KHCO_3$	-0.8 V / 4.5 mA/cm^2 -0.9 V / 5.0 mA/cm^2	C_2H_4 2.3%, EtOH 1.7%, *n*-PrOH 0.6% C_2H_4 13.4%, EtOH 5.7%, *n*-PrOH 2.4%	Ref. 10
Cu(I) oxide films (1.7μm film)	0.1M $KHCO_3$	-0.85 V / n/a	C_2H_4 13.3%, EtOH 1.5%	Ref. 11
Agglomerated Cu nanoparticles (oxide-reduced)	0.1M $KHCO_3$	-0.85 V / 6.2 mA/cm^2	C_2H_4 18.14%, EtOH 4.43%, *n*-PrOH 7.44%	Ref. 12
Plasma-treated Cu foil (O_2 20W 2min)	0.1M $KHCO_3$	-0.86 V / 10.7 mA/cm^2	C_2H_4 46.1%	Ref. 13
Cu_2O derived Cu films	0.1M $KHCO_3$	-0.88 V / 12.7 mA/cm^2	C_2H_4 15%, EtOH 7.8%, *n*-PrOH 7.8%	Ref. 14

(sample C)				
Cu NP/N-doped graphene	0.1M $KHCO_3$	-0.9 V / 0.4 mA/cm^2	-[a]	Ref. 15
oxide-derived Cu_4Zn film	0.1M $KHCO_3$	-0.85 V / 10.1 mA/cm^2	C_2H_4 0.24%, EtOH 0.62%, *n*-PrOH 0.12%	Ref. 16
O_2-plasma treated CuO_xCl_y cubes (on Cu foil)	0.1M $KHCO_3$	-0.82 V / 7.6 mA/cm^2	C_2H_4 20.4%, EtOH 4.9%, *n*-PrOH 3.7%	Ref. 17

[a]no C_2-C_3 products, only C_1

Table S6. Comparison of optimized C_2-C_3 product formation from various Cu-based heterogeneous catalysts in neutral pH aqueous media.

	Electrolyte	V (vs. RHE) / j_{Total} (mA/cm^2)	C_2-C_3 product FE (%)	Ref.
trans-CuEn	0.1M $KHCO_3$	-0.86 V / 20.4 mA/cm^2	C_2-C_3 products 55.2% C_2H_4 33.2%, EtOH 16.6%, *n*-PrOH 3.5%	This work
trans-CuEn 2	0.1M $CsHCO_3$	-0.75 V / 21.7 mA/cm^2	C_2-C_3 products 49.3% C_2H_4 31.9%, EtOH 11.7%, *n*-PrOH 3.5%	This work
Cu foil	0.1M $KHCO_3$	-1.05 V / 5.8 mA/cm^2	C_2-C_3 products 40.6% C_2H_4 26%, EtOH 9.8%, *n*-PrOH 2.5%	Ref. 3
Cu_2O film derived Cu NPs	0.1M $KHCO_3$	-1.1 V / n/a	C_2H_4 33.5%	Ref. 4
Cu_2O derived Cu with $PdCl_2$	0.1M $KHCO_3$	-1.0 V / 19.5 mA/cm^2	C_2H_6 30.1%, EtOH 11.1%, *n*-PrOH 5.5%	Ref. 5
Electrodeposited Cu_2O on carbon	0.5M $KHCO_3$	-1.2 V / 9.1 mA/cm^2	C_2H_4 25.5%	Ref. 6
Cu mesocrystals (from CuCl film)	0.1M $KHCO_3$	-0.99 V / 25 mA/cm^2	C_2H_4 27.2%	Ref. 7
Cu_2O-Cu (Cl induced)	0.1M KCl	-1.8 V / 7.7 mA/cm^2	C_2-C_4 products 55.1% C_2H_4 23%, EtOH 20%, *n*-PrOH 7.8% C_3H_8 1%, C_4H_{10} 1%	Ref. 8
Oxide-derived Cu-foam	0.5M $NaHCO_3$	-0.8 V / 10.9 mA/cm^2	C_2 products 55% C_2H_4 20%, C_2H_6 35%,	Ref. 9
Nanostructured polycrystalline Cu (KF cycled)	0.1M $KHCO_3$	-1.0 V / 6.5 mA/cm^2	C_2-C_3 products 28% C_2H_4 16.3%, EtOH 7.85%, *n*-PrOH 3.08%	Ref. 10
Cu cubes (44nm size)	0.1M $KHCO_3$	-1.1 V / 3.0 mA/cm^2	C_2-C_3 products 50.1% C_2H_4 41.1%, EtOH 3.7%, *n*-PrOH 2.7%	Ref. 1
Cu(I) oxide film (1.7μm film)	0.1M $KHCO_3$	-0.99 V / 30 mA/cm^2	C_2H_4 38.79%, EtOH 9.01%	Ref. 11
Agglomerated Cu nanoparticles (oxide-reduced)	0.1M $KHCO_3$	-0.95 V / 19.9 mA/cm^2	C_2H_4 35.82%, EtOH 12.75%, *n*-PrOH 8.75%	Ref. 12
Plasma-treated Cu foil (O_2 20W 2min)	0.1M $KHCO_3$	-0.92 V / 19.9 mA/cm^2	C_2H_4 60%, EtOH 0.95%	Ref. 13

Cu_2O derived Cu films (sample C)	0.1M $KHCO_3$	-0.98 V / 26.2 mA/cm^2	C_2H_4 31%, EtOH 7.1%, *n*-PrOH 3.7%	Ref. 14
Cu NP/N-doped graphene	0.1M $KHCO_3$	-1.2 V / 1.2 mA/cm^2	EtOH 63%	Ref. 15
oxide-derived Cu_4Zn film	0.1M $KHCO_3$	-1.05 V / 37.3 mA/cm^2	C_2H_4 10.75%, EtOH 29.14%, *n*-PrOH 4.39%	Ref. 16
O_2-plasma treated CuO_xCl_y cubes (on Cu foil)	0.1M $KHCO_3$	-1.05 V / 49.7 mA/cm^2	C_2-C_3 products 64.6%[a] C_2H_4 39.7%, EtOH 20%, *n*-PrOH 4.4%	Ref. 17
Single crystals Cu (100)	0.1M $KHCO_3$	-1 V / 5 mA/cm^2	C_2-C_3 products 57.8% C_2H_4 40.4%, EtOH 9.7%, *n*-PrOH 1.5%	Ref. 18
Cu (711) / [4(100) × (111)]	0.1M $KHCO_3$	-0.94 V / 5 mA/cm^2	C_2-C_3 products 71.5% C_2H_4 50.0%, EtOH 7.4%, *n*-PrOH 4.6%	

[a]Total FE of all the products reported in the work is ~115%. The numbers shown here are corrected values after normalization.

Table S7. Comparison of ethylene-to-methane (C_2H_4/CH_4) ratio among various Cu-based heterogeneous catalysts in neutral pH aqueous media.

	Electrolyte	**Potential (V vs. RHE)**	**C_2H_4/CH_4 ratio[a]**	**Ref.**
trans-CuEn	0.1M $KHCO_3$	-0.78 V	252	This work
trans-CuEn 2	0.1M $CsHCO_3$	-0.73 V	2133	This work
Cu_2O film derived Cu NPs	0.1M $KHCO_3$	-	8 ~ 12	Ref. 4
Cu_2O derived Cu with $PdCl_2$	0.1M $KHCO_3$	-1.0 V	60[b]	Ref. 5
Electrodeposited Cu_2O on carbon	0.5M $KHCO_3$	-1.13 V	43	Ref. 6
Cu mesocrystals (from CuCl film)	0.1M $KHCO_3$	-0.89 V	86	Ref. 7
Cu_2O-Cu (Cl induced)	0.1M KCl	-1.8 V	19	Ref. 8
Nanostructured polycrystalline Cu (KF cycled)	0.1M $KHCO_3$	-1.0 V	51	Ref. 10
Cu cubes (44nm size)	0.1M $KHCO_3$	-1.0 V	6	Ref. 1
Cu(I) oxide films	0.1M $KHCO_3$	-0.99 V	~100	Ref. 11
Agglomerated Cu nanoparticles (oxide-reduced)	0.1M $KHCO_3$	-0.85 V	360	Ref. 12
Plasma-treated Cu foil (O_2 20W 2min)	0.1M $KHCO_3$	-0.81 V	108	Ref. 13
Cu NP/N-doped graphene[b]	0.1M $KHCO_3$	-1.2 V	9.4[b]	Ref. 15
oxide-derived Cu_4Zn film[b]	0.1M $KHCO_3$	-1.05 V	69[b]	Ref. 16
O_2-plasma treated CuO_xCl_y cubes (on Cu foil)	0.1M $KHCO_3$	-0.82 V	25	Ref. 17

Single crystals Cu (100)	0.1M $KHCO_3$	-1 V	1.3	Ref. 18
Cu (711) / [4(100) × (111)]	0.1M $KHCO_3$	-0.94	10.0	

[a]As Cu-based catalysts capable of producing multi-carbon products often have lower onset potentials for ethylene compared to methane, comparisons are made for cases where C_2H_4 FE > 15%, to ensure that catalysts are producing certain amount of C_2H_4. (Otherwise, even with very low C_2H_4 FE, the ratio can be high when there is negligible amount of CH_4) The value shown is the highest among the ones across a certain potential regime for each catalyst.
[b]C_2H_6/CH_4 or $EtOH/CH_4$ ratio

Table S8. Faradaic efficiencies of various products observed for trans-CuEn 2 in 0.1 M $CsHCO_3$ at 1 atm CO_2.

	-0.53 V / 1.6 mA/cm$^2_{geo}$	**-0.57 V / 2.2 mA/cm$^2_{geo}$**	**-0.62 V / 3.0 mA/cm$^2_{geo}$**	**-0.66 V / 4.6 mA/cm$^2_{geo}$**	**-0.73 V / 9.6 mA/cm$^2_{geo}$**	**-0.75 V / 21.7 mA/cm$^2_{geo}$**	**-0.79 V / 24.7 mA/cm$^2_{geo}$**
C_1	25.4 %	37.1 %	42.8 %	35.1 %	17.9 %	7.7 %	4.7 %
CO	20.3 %	24.3 %	23.2 %	16.8 %	7.7 %	3.0 %	1.6 %
CH_4	-	-	-	-	*trace*	0.1 %	0.5 %
$HCOO^-$	4.9 %	12.6 %	19.4 %	18.2 %	10.2 %	4.6 %	2.6 %
MeOH	0.1 %	0.2 %	0.2 %	*trace*	*trace*	*trace*	*trace*
C_2	4.4 %	7.1 %	11.7 %	19.1 %	36.5 %	45.0 %	40.0%
C_2H_4	2.3 %	3.7 %	5.9 %	10.2 %	22.9 %	31.9 %	27.4 %
C_2H_6	0.3 %	0.6 %	1.0 %	1.1 %	1.1 %	0.3 %	0.1 %
EtOH	1.7 %	1.4 %	2.5 %	5.0 %	10.1 %	11.7 %	11.5 %
Acetaldehyde	-	0.4%	1.0 %	1.2 %	0.6 %	0.3 %	0.3 %
Acetate	*trace*	0.9 %	1.3 %	1.6 %	1.4 %	0.6 %	0.4 %
Glycolaldehyde	-	-	-	-	0.3 %	0.3 %	0.3 %
C_3	0.6 %	1.3 %	3.1 %	4.8 %	6.1 %	4.3 %	3.0 %
Acetone	0.2 %	0.1 %	0.1 %	0.1 %	0.2 %	0.1 %	0.1 %
n-PrOH	0.4 %	1.2 %	2.7 %	4.7 %	5.3 %	3.5 %	2.5 %
Allyl alcohol	-	-	0.3 %	*trace*	0.7 %	0.6 %	0.5 %
H_2	69.5 %	54.5 %	42.4 %	41.0 %	39.5 %	43.0 %	52.3 %

Table S9. Standard reduction potentials and overpotentials (at -0.75 V vs. RHE) for various CO_2 reduction products observed in this work. Values are from refs 3, 19-22.

Products	**Standard reduction potential (V vs. RHE)**	**Thermodynamic potential (with OER)**	**Overpotential (-0.75 V vs. RHE)**
CO	-0.11 V	1.34 V	0.64 V
CH_4	0.17 V	1.06 V	0.92 V
$HCOO^-$	-0.02 V	1.25 V	0.73 V
MeOH	0.03 V	1.20 V	0.78 V
C_2H_4	0.07 V	1.16 V	0.82 V
C_2H_6	0.14 V	1.09 V	0.89 V
EtOH	0.08 V	1.15 V	0.83 V
Acetaldehyde	0.05 V	1.18 V	0.80 V
Acetate	0.14 V	1.09 V	0.89 V
Glycolaldehyde	-0.03 V	1.26 V	0.72 V
Acetone	0.10 V	1.13 V	0.85 V
n-PrOH	0.10 V	1.13 V	0.85 V
Allyl alcohol	0.05 V	1.18 V	0.80 V
Propionaldehyde	0.09 V	1.14 V	0.84 V

References

1. Loiudice A, et al. (2016) Tailoring Copper Nanocrystals towards C_2 Products in Electrochemical CO_2 Reduction. *Angew Chemie Int Ed* 55(19):5789–5792.

2. Vermaas DA, Smith WA (2016) Synergistic Electrochemical CO_2 Reduction and Water Oxidation with a Bipolar Membrane. *ACS Energy Lett* 1(6):1143–1148.

3. Kuhl KP, Cave ER, Abram DN, Jaramillo TF (2012) New insights into the electrochemical reduction of carbon dioxide on metallic copper surfaces. *Energy Environ Sci* 5(5):7050.

4. Kas R, et al. (2014) Electrochemical CO_2 reduction on Cu_2O-derived copper nanoparticles: controlling the catalytic selectivity of hydrocarbons. *Phys Chem Chem Phys* 16(24):12194.

5. Chen CS, Wan JH, Yeo BS (2015) Electrochemical Reduction of Carbon Dioxide to Ethane Using Nanostructured Cu_2O-Derived Copper Catalyst and Palladium(II) Chloride. *J Phys Chem C* 119(48):26875–26882.

6. Kim D, et al. (2015) Insights into an autonomously formed oxygen-evacuated Cu_2O electrode for the selective production of C_2H_4 from CO_2. *Phys Chem Chem Phys* 17(2):824–830.

7. Chen CS, et al. (2015) Stable and selective electrochemical reduction of carbon dioxide to ethylene on copper mesocrystals. *Catal Sci Technol* 5(1):161–168.

8. Lee S, Kim D, Lee J (2015) Electrocatalytic Production of C3-C4 Compounds by Conversion of CO_2 on a Chloride-Induced Bi-Phasic Cu_2O-Cu Catalyst. *Angew Chemie Int Ed* 54(49):14701–14705.

9. Dutta A, Rahaman M, Luedi NC, Mohos M, Broekmann P (2016) Morphology Matters: Tuning the Product Distribution of CO_2 Electroreduction on Oxide-Derived Cu Foam Catalysts. *ACS Catal* 6(6):3804–3814.

10. Kwon Y, Lum Y, Clark EL, Ager JW, Bell AT (2016) CO_2 Electroreduction with Enhanced Ethylene and Ethanol Selectivity by Nanostructuring Polycrystalline Copper. *ChemElectroChem* 3(6):1012–1019.

11. Ren D, et al. (2015) Selective Electrochemical Reduction of Carbon Dioxide to Ethylene and Ethanol on Copper(I) Oxide Catalysts. *ACS Catal* 5(5):2814–2821.

12. Ren D, Wong NT, Handoko AD, Huang Y, Yeo BS (2016) Mechanistic Insights into the Enhanced Activity and Stability of Agglomerated Cu Nanocrystals for the Electrochemical Reduction of Carbon Dioxide to n-Propanol. *J Phys Chem Lett* 7(1):20–24.

13. Mistry H, et al. (2016) Highly selective plasma-activated copper catalysts for carbon dioxide reduction to ethylene. *Nat Commun* 7:12123.

14. Handoko AD, et al. (2016) Mechanistic Insights into the Selective Electroreduction of Carbon Dioxide to Ethylene on Cu_2O-Derived Copper Catalysts. *J Phys Chem C* 120(36):20058–20067.

15. Song Y, et al. (2016) High-Selectivity Electrochemical Conversion of CO_2 to Ethanol using a Copper Nanoparticle/N-Doped Graphene Electrode. *ChemistrySelect* 1(19):6055–6061.

16. Ren D, Ang BS-H, Yeo BS (2016) Tuning the Selectivity of Carbon Dioxide Electroreduction toward Ethanol on Oxide-Derived Cu_xZn Catalysts. *ACS Catal* 6(12):8239–8247.

17. Gao D, et al. (2017) Plasma-Activated Copper Nanocube Catalysts for Efficient Carbon Dioxide Electroreduction to Hydrocarbons and Alcohols. *ACS Nano* 11(5):4825–4831.

18. Hori Y, Takahashi I, Koga O, Hoshi N (2003) Electrochemical reduction of carbon dioxide at various series of copper single crystal electrodes. *J Mol Catal A Chem* 199(1–2):39–47.

19. Brown, M. *et al. Sustainable Bioenergy and Bioproducts*. (Springer London, 2012). doi:10.1007/978-1-4471-2324-8

20. Haynes, W. M. *CRC Handbook of Chemistry and Physics*. (CRC Press, 2016).

21. Speight, J. G. *Lange's Handbook of Chemistry*. (McGraw-Hill Education, 2017).

22. Hori, Y. in *Modern Aspects of Electrochemistry* 89–189 (Springer New York, 2008). doi:10.1007/978-0-387-49489-0_3